Journal of Applied Geophysics 161 (2019) 56–75

Contents lists available at ScienceDirect

Journal of Applied Geophysics

journal homepage: www.elsevier.com/locate/jappgeo

Delineation of a buried volcanic system in Kora prospect off New Zealand using artificial neural networks and its implications

Priyadarshi Chinmoy Kumar [a,b], Kalachand Sain [a,b,c,*], Animesh Mandal [d]

[a] CSIR-National Geophysical Research Institute, Uppal Road, Hyderabad, India
[b] Academy of Scientific and Innovative Research (AcSIR)-NGRI, India
[c] Wadia Institute of Himalayan Geology, Dehradun, Uttarakhand 248001, India
[d] Department of Earth Sciences, Indian Institute of Technology, Kanpur, India

ARTICLE INFO

Article history:
Received 15 April 2018
Received in revised form 19 November 2018
Accepted 22 December 2018
Available online 28 December 2018

Keywords:
Meta-attributes
Neural Networks
New Zealand
Taranaki basin

ABSTRACT

The Kora volcano, a submarine Miocene andesitic stratovolcano, is documented to be buried below ~1700 m sedimentary strata in the northern Taranaki basin off New Zealand. The buried volcano and enclosing older sedimentary strata, structurally modulated the subsurface architecture leading to the formation of structural and stratigraphic traps for hydrocarbon reservoirs. The Kora field is known for accumulating sub-commercial hydrocarbon resources within the volcanogenic deposits. Here, we attempt to image such a complex geological system from 3D time-migrated seismic data using state-of-the-art artificial neural networks coupled with interpreter's acquaintances. For this, we have computed several attributes; optimally amalgamated these and trained over interpreter's intelligence. This has resulted into a single new attribute, defined as the intrusion cube (IC) meta-attribute, to produce the best possible image of the subsurface. The resultant IC meta-attribute has successfully brought out the extension and distribution of volcanic edifice within the buried volcanic system along with several structural elements such as the sill networks, dyke swarms, forced folds, drag folds, jacked up strata and pinch-outs (along flanks of the volcano) in the host sedimentary successions, which are very essential in understanding the petroleum system of the Kora field. This interpretational approach, based on a blended output of neural intelligence of artificial networks and interpreters' knowledge, can be suitably employed for imaging any complex volcanic system from 3D seismic data.

1. Introduction

Volcanic systems are defined as a set of interconnected geologic structures that confines a complete magmatic-sedimentary complex (Bischoff et al., 2017), consisting of premagmatic sedimentary sequence deformed by magmatism, synintrusive, syneruptive and intereruptive part of a volcano along with the deformed sediments that buried them. These systems accompanied with the igneous and sedimentary processes may have both positive and negative impacts over the petroleum system, e.g., maturity of the source rocks; migration pathways for hydrocarbons; sealing and trapping mechanisms; geothermal history of the basin etc. (Allis et al., 1995; Farrimond et al., 1999; Stagpoole and Funnell, 2001; Schutter, 2003; Planke et al., 2005; Rohrman, 2007; Rateau et al., 2013; Zou, 2013; Sun et al., 2014). This type of complexities sometimes changes the porosity and permeability of subsurface reservoirs and poses high risks for exploration. Such complex geological system should be examined critically for the exploration of hydrocarbons. As discovery of oil/gas at ease is almost over, oil industries peep into difficult terrains like this for commercial gains.

High quality 3-D seismic reflection data is very reliable for delineating detailed architecture of these buried geological structures (Smallwood and Maresh, 2002; Cartwright and Hansen, 2006; Thomson and Schofield, 2008; Polteau et al., 2008; Rateau et al., 2013; Sun et al., 2014; Magee et al., 2015). Such intrusive features like volcanoes, sills, dykes etc., are usually well-imaged due to their high amplitude character (which is a function of density and velocity), abrupt lateral terminations and complex geometries within the host-rock strata (Smallwood and Maresh, 2002; Planke et al., 2005; Alves et al., 2015). However, imaging of 3-D seismic reflection data by conventional processing suffers some limitations due to (a) reduction in seismic quality and resolution with depth, (b) overburden effects, (c) noise in complex areas that potentially masks many geologic structures and (d) inability to image steeply dipping and vertical interfaces (Thomson and Schofield, 2008; Jackson et al., 2013; Planke et al., 2005; Eide et al., 2017).

Several advanced interpretation tools such as manual interpretation, geo-bodies extraction, volume blending techniques (Chaves et al., 2011; Holford et al., 2012; Alves et al., 2015; Bischoff et al., 2017) and facies

* Corresponding author at: CSIR-National Geophysical Research Institute, Uppal Road, Hyderabad, India.
E-mail addresses: kalachandsain@yahoo.com (K. Sain), animeshm@iitk.ac.in (A. Mandal).

https://doi.org/10.1016/j.jappgeo.2018.12.008
0926-9851/

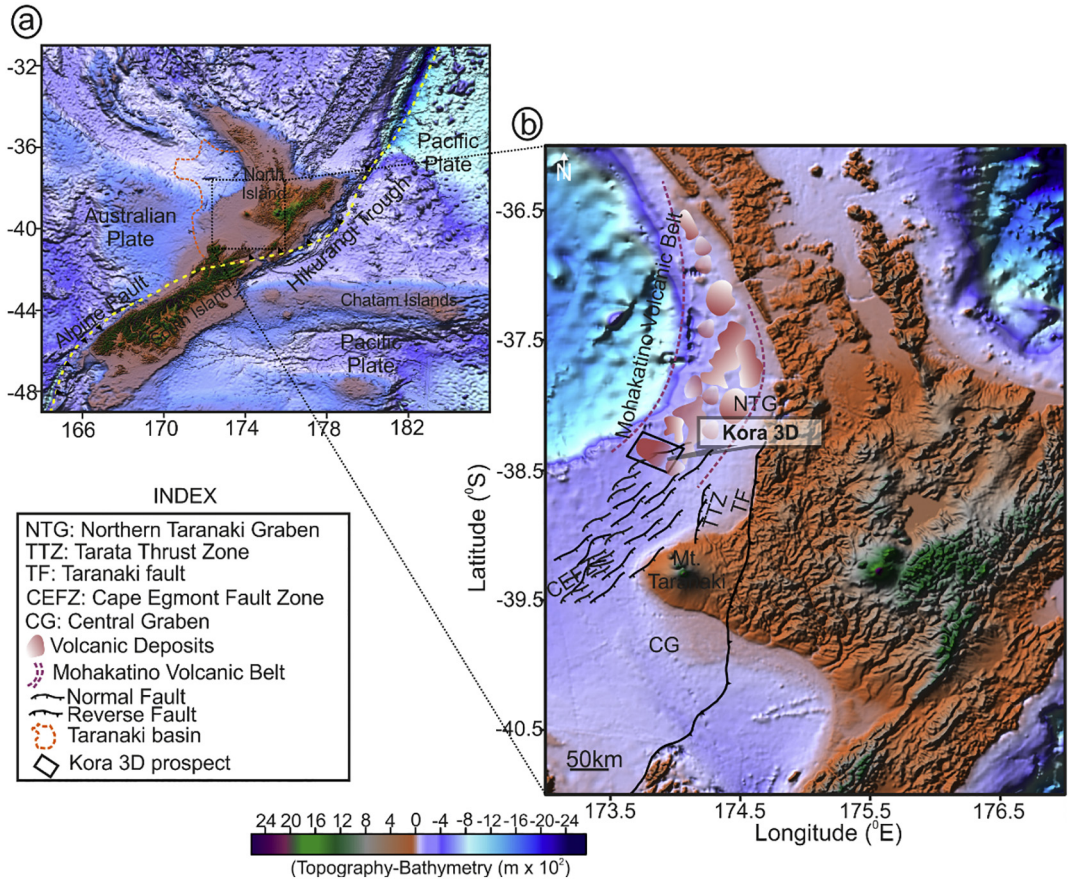

Fig. 1. (a) Topography-bathymetry illustrating the tectonic plates e.g., Australian Plate, Pacific Plate, Alpine Fault system and the Hikurangi Trough. Please see the Index for the location of Taranaki Basin (orange dotted polygon) and other key structural elements; (b) The Kora 3D prospect, covering an area of 720 km^2 in the northern part of the Taranaki Basin, is indicated by a black rectangular box. The Kora field, one of the volcanic complexes lying within the Mohakatino Volcanic Belt, was active during the Miocene period.

analysis (Infante-Paez and Marfurt, 2017), have been employed for the delineation of such complex geological system along with their subsurface disposition. The role of seismic attribute analysis in this regard is often laudable (Jiang et al., 2004; Pena et al., 2009; Zhang et al., 2011; Cortez and Cetale Santos, 2016, Alves et al., 2015). Several attributes such as the similarity, coherence, dip-azimuth, reflection strength, seismic textures, curvature, impedance inversion (Chopra and Marfurt, 2007; Zuo and Fan, 2011) are efficient in illuminating intrusive bodies from seismic data.

The process of defining seismic attributes for illuminating the interpretation targets essentially depends on different parameters like the step-outs, time windows, input data etc. In such scenario, very often

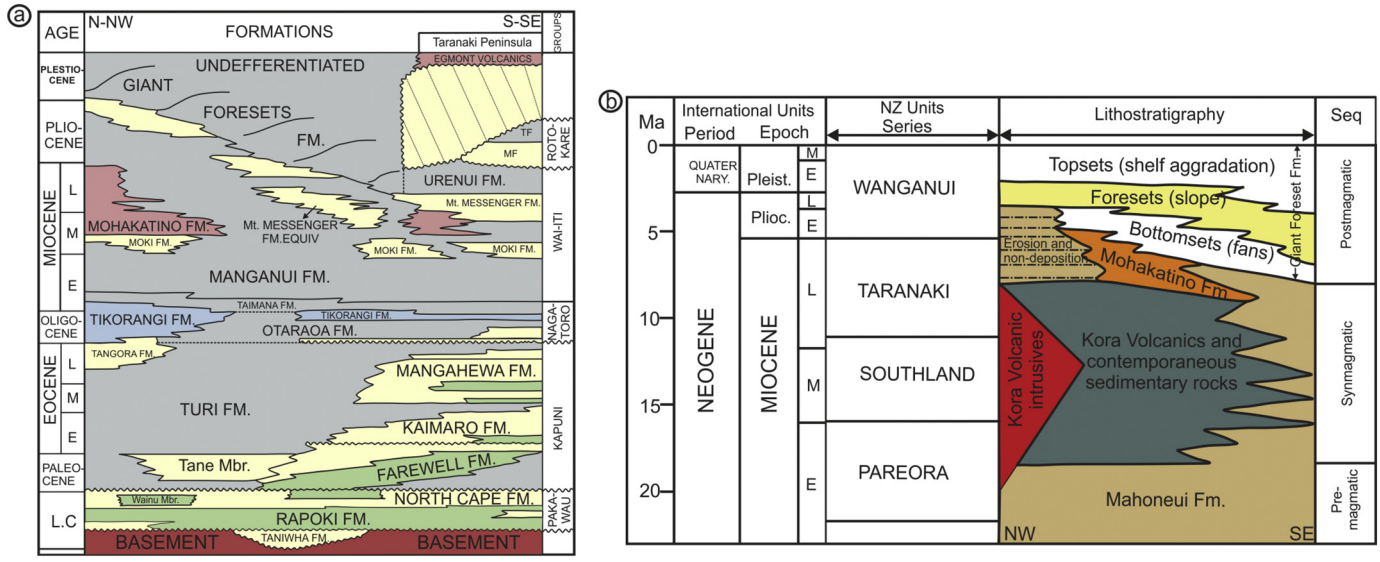

Fig. 2. (a) The Lithostratigraphy of Taranaki Basin demonstrating the evolution stratigraphic formations over the geological period; (b) The Neogene distribution of Kora volcanics and associated sedimentary formations within the prospect area. (*Modified after* Bergman et al., 1992;*King and Thrasher,* 1996).

interpreters encounter problems where (i) targeted geologic objects may not honour each of the extracted attributes and (ii) the attributes fail to discriminate geologic targets from the surroundings. Moreover, attributes hardly ever respond to a unique geologic feature. Hence, geo-bodies extraction from an attribute volume (e.g., envelope) mostly results into a mixture of overlapping responses of several geological features and noises, and thus the interpretation targets may not be highlighted. Additionally, steeply inclined or vertically intruding nature of geological objects becomes tedious to capture in geo-bodies extraction techniques (Bischoff et al., 2017). A possible way to overcome these difficulties in seismic interpretation could be the use of intensive computer-oriented algorithms that could enhance the data within the interval of interest and simplify interpretation tasks.

We attempt to improve the interpretation strategies by introducing a novel automated approach that integrates several seismic attributes coupled with interpreter's acquaintances such that the extension and

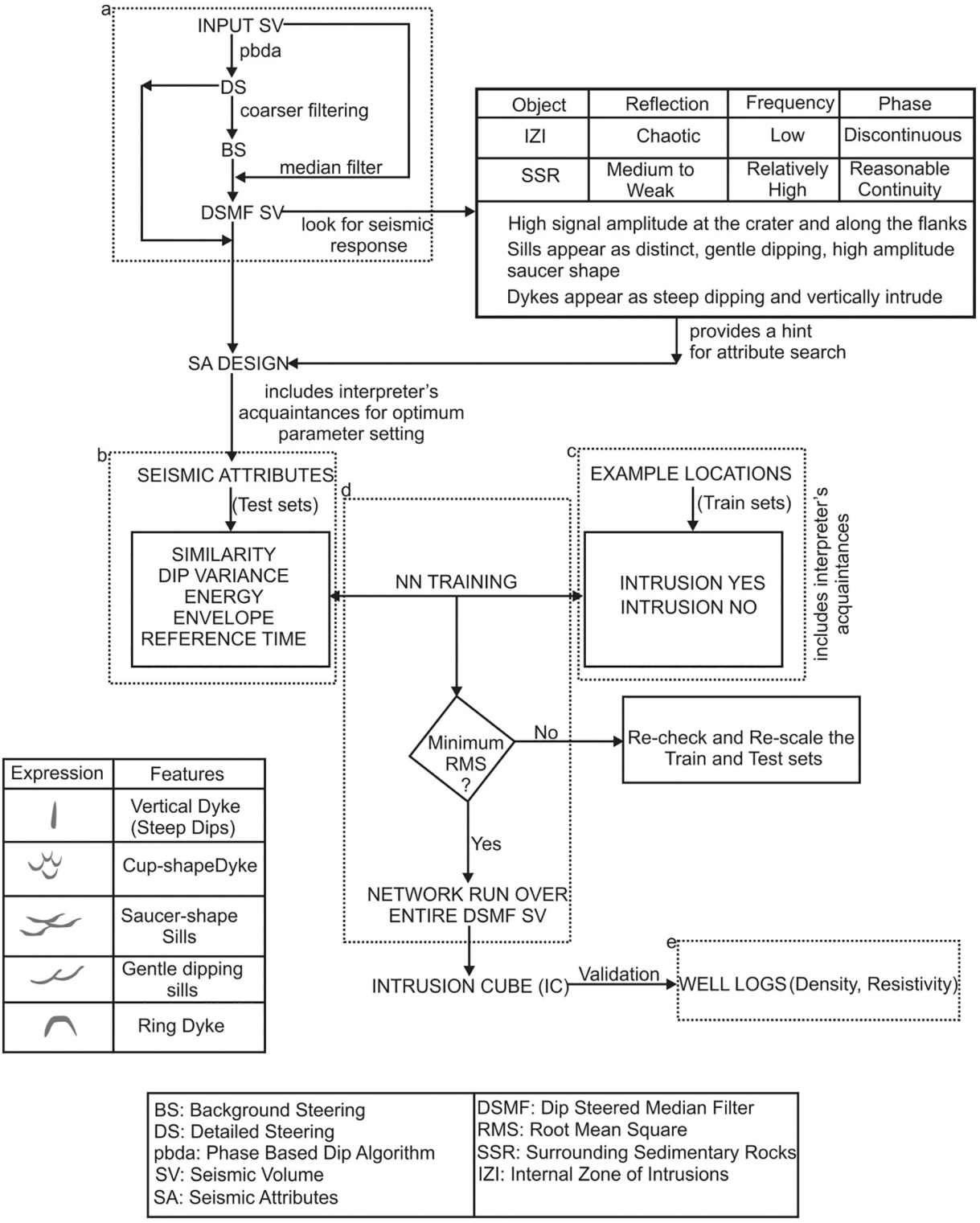

Fig. 3. Workflow adopted for designing the IC meta-attribute. Several expressions of intrusive features hint for interpretation targets (*Modified after* Mathieu et al., 2008). Apart from the main attributes mentioned in the workflow, several other attributes, as shown in the tables, are also used.

Table 1
Key seismic attributes and their parameter settings for generating an optimized IC meta-attribute.

Seismic Attributes	Filter properties				Documented Works
	Input Data	Time Window	Trace Position	Other Settings	
Similarity	DSMF Seismic Volume and Detailed Steering Seismic	[−32,+32] ms	(−1,0) &(1,0) 90^0 rotated	Minimum Similarity is the output	Tingdahl and de Rooij (2005), Singh et al. (2016), Kumar and Mandal (2017), Kumar and Sain (2018)
Coherency	DSMF Seismic Volume and Steering Seismic	[−12, +12] ms [−32,+32] ms	Cross Extension with 1 × 1 step-out	Minimum Coherency is the output	Chopra and Marfurt (2007)Kumar and Sain (2018)
Energy	DSMF Seismic Volume	[−50, +50] ms [−80, +80] ms [−40, +40] ms	----------	----------	Chopra and Marfurt (2007), Aminzadeh and de Groot (2006), Tingdahl and de Rooij (2005), Singh et al. (2016)
Dip Angle	Detailed Steering Seismic	----------	----------	----------	Chopra and Marfurt (2007), Tingdahl and de Rooij (2005), Singh et al. (2016), Kumar and Sain (2018)
Azimuth	Detailed Steering Seismic	----------	----------	----------	Chopra and Marfurt (2007), Tingdahl and de Rooij (2005), Singh et al. (2016), Kumar and Sain (2018)
Dip Angle Variance	Dip Angle	[−12. +12] ms [−32, +32] ms	Cube with 5 × 5 step-out	Variance is the output statistic	Aminzadeh and de Groot (2006) Tingdahl and de Rooij (2005)
Envelope	DSMF Seismic Volume	----------	----------	Instantaneous amplitude is the output	Chopra and Marfurt (2007), Barnes (2016), Kumar et al. (2019)
Reference Time	DSMF Seismic Volume	----------	----------	Time Value is the output	Singh et al. (2016), Kumar and Mandal (2017), Kumar and Sain (2018)

distribution of subsurface geologic targets like the buried volcanic system within the Kora field of New Zealand's Taranaki basin (Fig. 1) can be well defined by designing a new attribute, called the intrusion cube (IC) meta-attribute. This is obtained by amalgamating appropriate seismic attributes, sensitive to the targeted geologic objects. The ground truth of the findings has been validated with the available borehole data from the prospect. The IC meta-attribute is a novel concept of its own that illuminates the structural geometry (distribution and extension) of buried magmatic sedimentary complex from seismic data and streamlines the existing interpretation strategies for petroleum prospect point of view.

2. Geology and tectonics

Taranaki basin (TB), the main petroleum producing zone in New Zealand, lies in the western offshore of the North Island of New Zealand. It is ~60 km wide and extends ~350 km in NNE direction from south of Taranaki peninsula to offshore west of Auckland (Giba et al., 2010). The basin forms part of the overriding Australian plate and lies about ~400 km west of the Hikurangi Trough where the Pacific plate is subducted (Fig. 1a) (Giba et al., 2012; King and Thrasher, 1996). It has a multiphase deformation history with an extension during the Late Cretaceous to Early Eocene followed by compression regime from the Late Eocene to Recent and back-arc extension from the Late Miocene to Recent (Giba et al., 2012). The eastern part of the basin is bounded by the Taranaki Fault (Fig. 1b) and is covered by the Late Miocene and Pliocene sediments, whereas the western part imparts its extension beyond the present day continental shelf (King and Thrasher, 1996). The evolution of the TB dates back to the Late Cretaceous, which was associated with the breakup of Gondwanaland and the formation of the Tasman Sea giving rise to the fault bounded graben and half graben structures. These structures were filled by *syn*-rift sediments comprising interbedded coal measures and sandstone sequences of the Pakawau Group (Fig. 2a) (Palmer and Andrews, 1993; King and Thrasher, 1996). Thereafter, the basin underwent a major transgression overlying the Paleocene and Eocene deposits of post-rift and late-rift transgressive sedimentary sequences (King and Thrasher, 1996; Higgs et al., 2012). This event led to the deposition of terrestrial to marginal marine sequences of the Kapuni Group (Farewell, Kaimiro, Mangahewa and McKee Formations) (Fig. 2a) (Higgs et al., 2012). Inactive tectonism and reduction in clastic sediment supply during the Oligocene period formed widespread deposition of limestones and calcareous mudstones of the Ngatoro Group (Otaraoa and Tikorangi Formations) throughout the basin (King et al., 1999; King, 2000). Transgressive phase reached to its climax in the early Miocene (Ngatoro Group: Taimana formation and Wai-iti Group: Manganui formation) and regressive phase started from the Mid-Miocene consisting of the Wai-iti Group (Moki, Mokau, Mohakatino Formations) through the Pliocene Rotokare Group (Giant Foreset formation) to the present day (Higgs et al., 2012; Singh et al., 2016).

2.1. Kora volcano and its geology

The Kora volcano (a faulted conical submarine volcano) belongs to the part of a chain of >25 buried Miocene stratovolcanoes distributed within a NNE trending belt called as the Mohakatino Volcanic Belt (MVB) that lies close to the Northern Taranaki Graben (NTG) in the TB (Fig. 1b). The volcanoes within the MVB are attributed to be a part of the intraarc system developed due to the dehydration of the westward subducting Pacific plate beneath the Australian plate (King and Thrasher, 1996; Seebeck et al., 2014; Bischoff et al., 2017). The SW dipping subduction zone in the northern part of New Zealand, uplifted and exposed large areas of the Zealandia during the Neogene period, providing enormous sediment supply to the neighboring sedimentary basins. This has received the deposition of thick sedimentary sequences in offshore NTG. The stratovolcanoes of the MVB got buried by the shelf prograding sedimentary piles about ~20 Ma ago, thereby producing a thick basin fill during the Neogene period (Fig. 2b). These basin fill sediments locally interfingered with the volcanic rocks and volcanoclastic sediments of the MVB (King and Thrasher, 1996; Stagpoole and Funnel, 2001; Bischoff et al., 2017). The Kora volcano evolved on the deep water mudstones of Early Miocene (18.70–15.90 Ma) (Bischoff et al., 2017) and the Mahoeuni interval (Fig. 2b). The Kora volcano has been sampled by five exploration wells (ARCO, 1988). Geochemical analysis of recovered samples revealed that the volcanic rocks comprise mainly low to medium potash, calc-alkaline and basaltic andesites (Stagpoole and Funnell, 2001; Bischoff et al., 2017). This suggests that magma was derived from the partial melts of the asthenospheric mantle and was not contaminated by the continental crust during the rise of magma (Bergman et al., 1992; Stagpoole and Funnell, 2001; Bischoff

Table 2
Neural network parameters used for three different IC meta-attribute models.

Neural Model	Neurons in different layers			Learning Rate	Momentum	Bias
	Input Layer	Hidden Layer	Output Layer			
IC Case I	9	5	2	0.01	0.25	1
IC Case II	10	5	2	0.01	0.25	1
IC Case III	9	5	2	0.01	0.25	1

et al., 2017). The Kora volcanic eruptions continued from a period of 14 Ma–8 Ma (King and Thrasher, 1996; Stagpoole and Funnell, 2001) (Fig. 2b). The flanks of the Kora edifice are onlapped by volcanoclastic sediments and prograding marine sediments of the Giant Foreset interval near its crest (Fig. 2b). Later, the activity was ceased and the volcanic edifice was completely buried by 3.7–4.4 Ma (Bergman et al., 1992; King and Thrasher, 1996; Stagpoole and Funnell, 2001; Bischoff et al., 2017). The Kora prospect was explored and drilled by Arco Petroleum NZ Ltd. in mid-1980s (ARCO, 1988). The first drilled well Kora-1 penetrated a thick sequence of Miocene volcanoclastic rocks and was reported to produce over 1168 barrels of oil per day (bopd) for about 10 days. This discovery further led to a detailed exploration by subsequently drilling three more appraisal wells within the prospect area.

3. Geophysical data

The geophysical data for this study includes a high resolution 3D seismic data from the Kora prospect in offshore TB and logs from

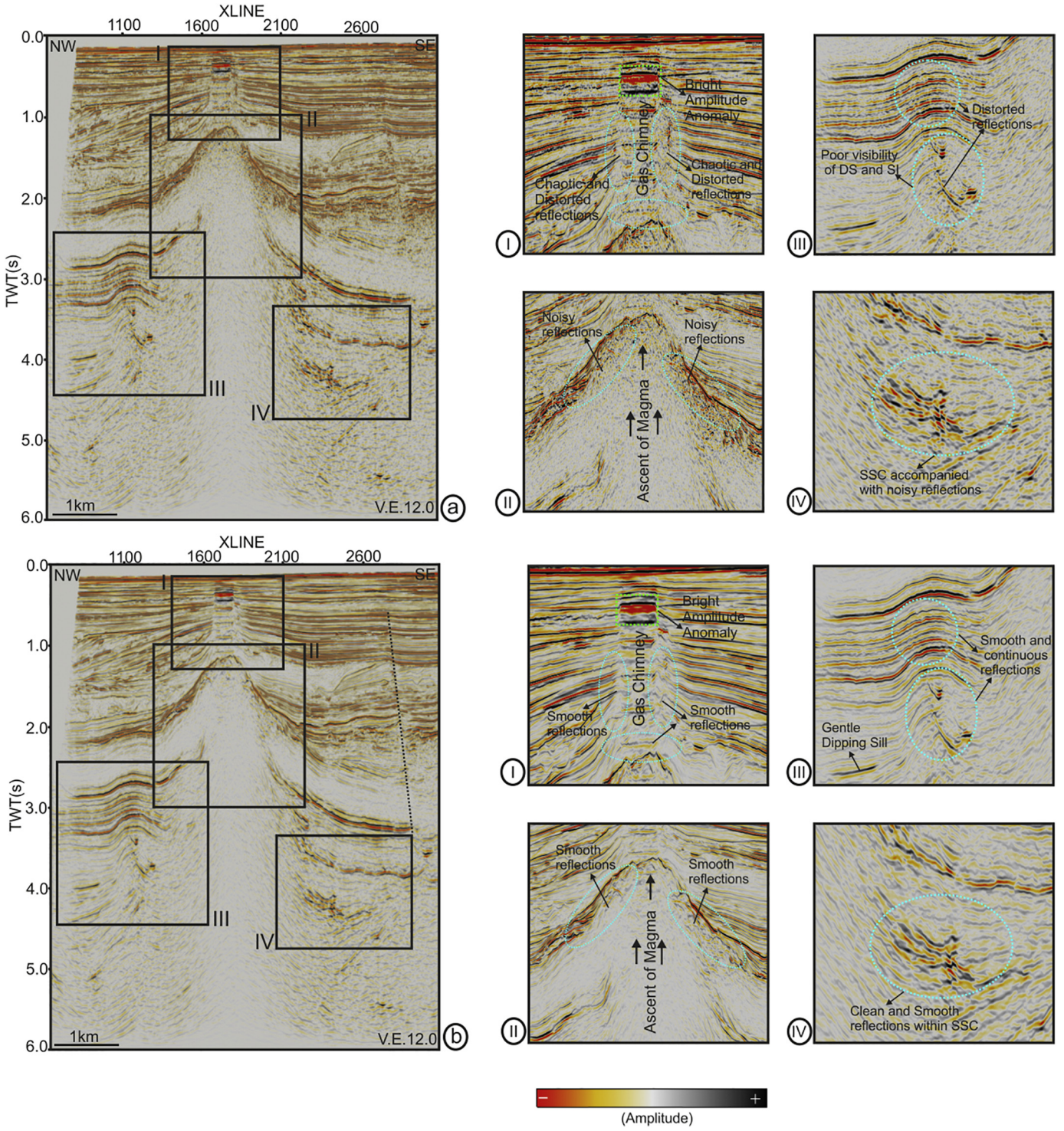

Fig. 4. (a) Original time-migrated seismic section for inline 1317 from the Kora 3D seismic volume. Seismic signals within the plumbing system are disturbed, as observed from four zoomed-in compartments (I, II, III and IV) displayed at immediate right; (b) DSMF time-migrated seismic section for the same inline shows enhanced image of geologic features, as observed in four zoomed-in compartments (I, II, III and IV) at immediate right.

borehole Kora-1 drilled by ARCO petroleum. The 3-D time migrated seismic volume comprises 957 inlines (W-E) and 2482 xlines (N-S), acquired with 25.0 m × 12.5 m (inl/xl) bin size, 4 ms sampling interval (equivalent to Nyquist frequency of 125 Hz) and 6 s record length. The seismic data polarity is SEG standard. This means that an increase in acoustic impedance is reflected as peak or positive amplitude. A dominant frequency of 45 Hz, in the vicinity of volcanic crater and an assumed interval velocity of 5500 m/s (Skogly, 1998; Hansen and Cartwright, 2006), suggests that crater >30 m thick can be resolved (corresponding to the resolution limit of λ/4). Similarly, a dominant seismic frequency of 25 Hz suggests that sills >55 m thick can be resolved with discrete seismic reflections from its top and base contacts. The log data of Kora-1 borehole are used for validating the ground truth, and the findings are described below.

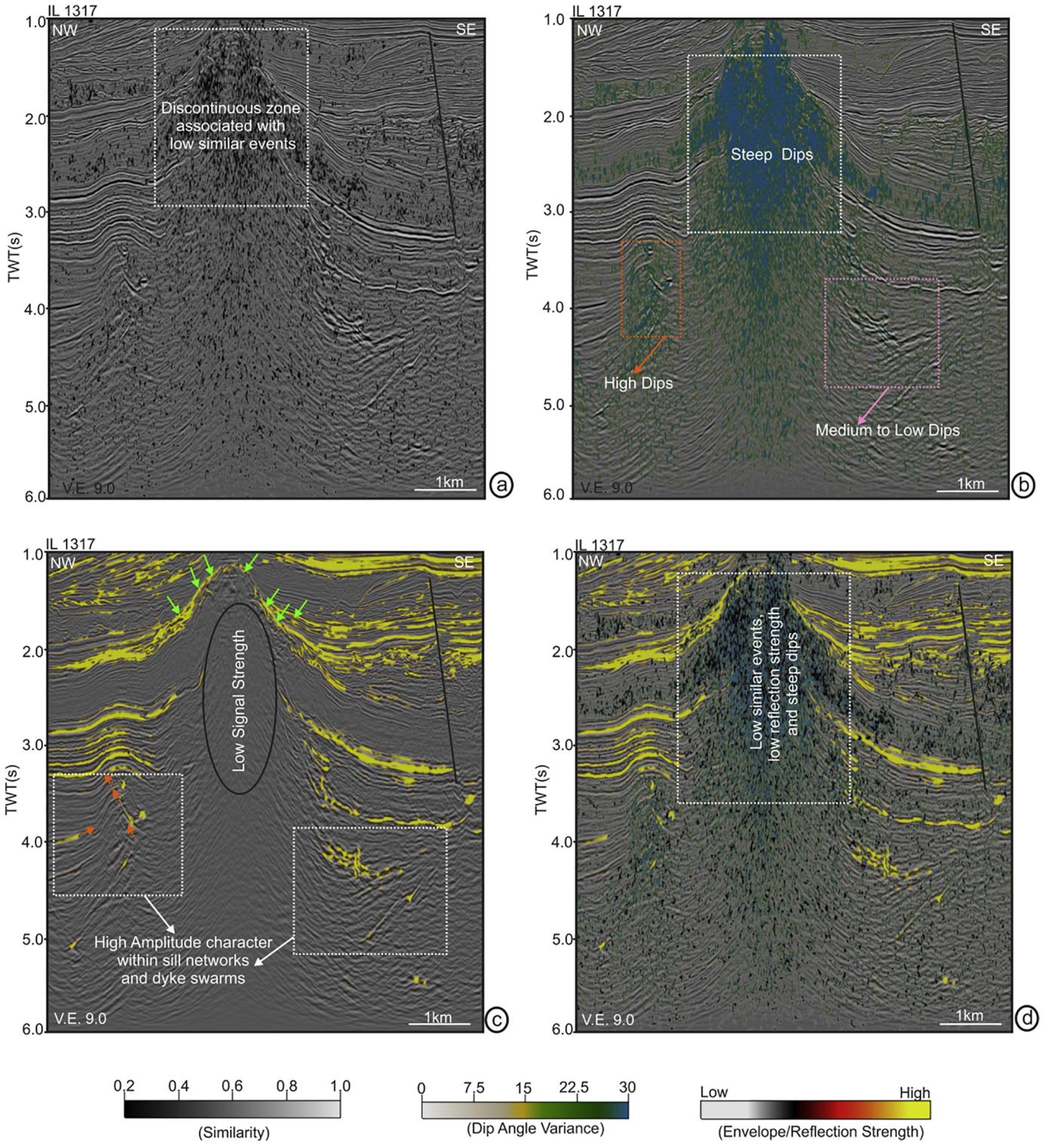

Fig. 5. Seismic attributes extracted from conditioned seismic data, displayed for inline 1317. (a) Similarity attribute co-rendered with the amplitude data; (b) Dip angle variance attribute co-rendered with the amplitude data; (c) Energy attribute co-rendered with amplitude data; (d) Co-rendered display of (a), (b) and (c) with the amplitude data. The section is fault marked (black line).

4. Methodology

The philosophy of defining a meta-attribute by logically combining a set of related attributes (extracted from seismic data) through artificial neural network was first proposed by Meldahl et al. (1999). This has brought a revolutionary change in the interpretation of seismic data. Following this, a new meta-attribute has been designed to effectively image the structural elements of the buried volcanic system along with their delimitation from high resolution 3D seismic data. The workflow (Fig. 3) consists of five main phases: (a) Data conditioning to improve the S/N ratio, (b) Extraction of related and suitable attributes from seismic data based on interpreter's acquaintances, (c) Selection of example locations based on interpreter's acquaintances, (d) Designing a logical neural network to define the required meta-attribute i.e., the IC volume, followed by (e) Validating the interpretation with other geophysical data such as the log data.

4.1. Data conditioning

Data conditioning or noise reduction is an important step to visualize the anomalous geological features on seismic section/volume. The data volume is optimally conditioned using a structurally-oriented filter (SOF) that utilizes pre-computed dip-azimuth volumes to steer the data in the direction of local dip of the seismic events (Tingdahl, 1999). This helps in improving the lateral continuity of seismic events and removes random noises from the data.

4.1.1. Extraction of dip through steering cube computation

The dip-azimuth extraction is carried out using a technique known as the dip-steering proposed by Tingdahl (1999). The technique uses local dip and azimuth of the seismic events to track the event locally with respect to the trace segments under investigation. The dip-steering process results in a steering cube (or a dip-azimuth volume) (Tingdahl, 1999; Tingdahl and de Groot, 2003; Jaglan et al., 2015; Kumar and Mandal, 2017; Kumar and Sain, 2018) that contains local dips of seismic reflections and associated discontinuities. The steering cube is computed using a phase-based dip algorithm (PBDA). Once the steering cube is computed, it is filtered using median filter both locally and regionally to check the quality and improvement of data for either of the two cases. A mild filtering step out i.e., inline: xline: sample: 1x1x3 is used to understand the local variations. The output, defined as the detailed steering (DS) cube,

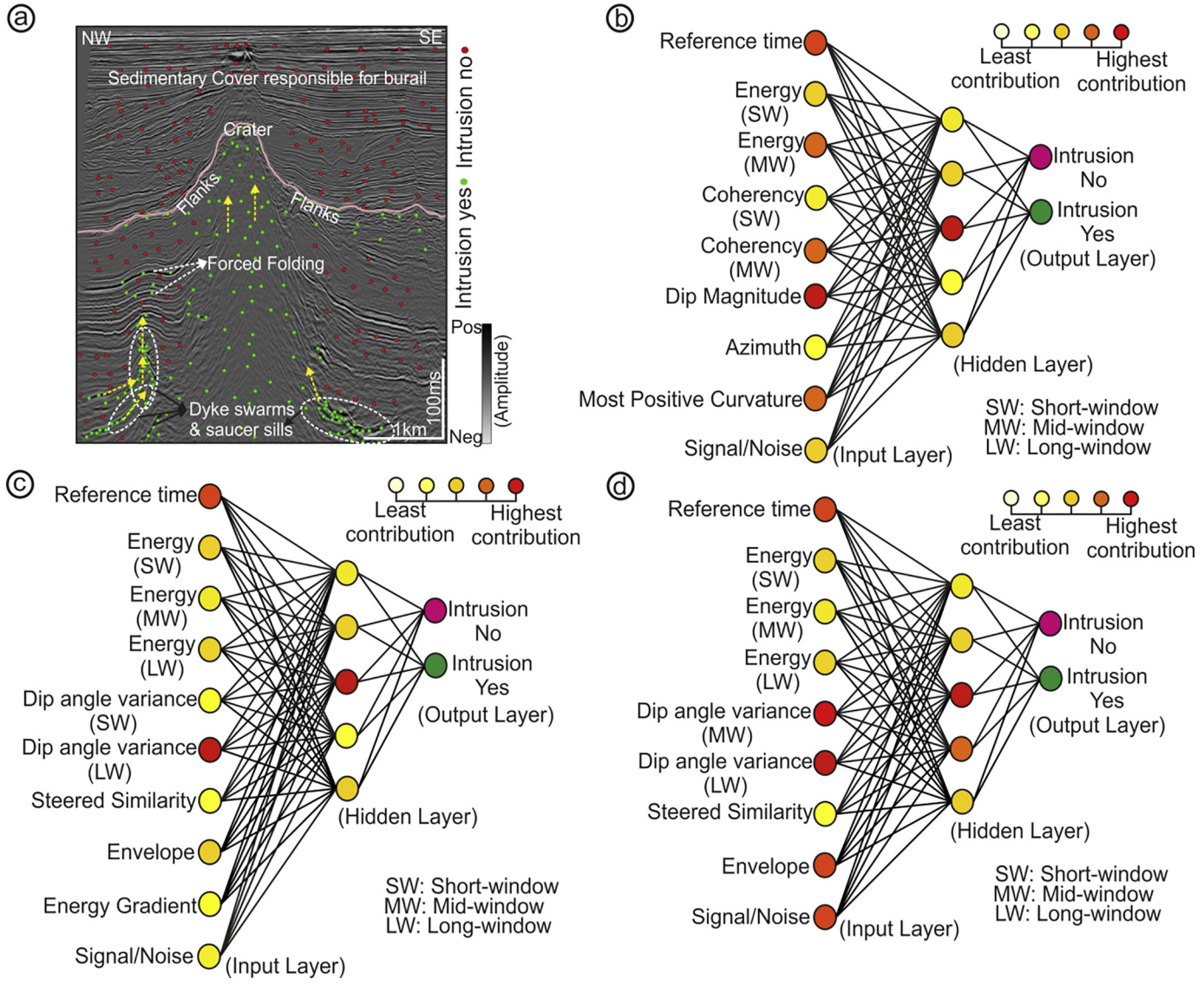

Fig. 6. (a) Picked example locations, displayed for inline 1317, are classified into intrusion-yes (green dots) and intrusion-no (red dots) groups. The designed MLP network for Case I (b), Case II (c) and Case III (d) consisting of three distinct interconnected layers: input, hidden and output layers respectively. (For interpretation of the references to colour in this figure legend, the reader is referred to the web version of this article.)

stores detailed information of seismic reflections. However, for defining the overall trend, coarser filtering is applied to the detailed steering cube using a filtering step out i.e., inline: xline: sample: 5x5x5. The resulting steering cube is called the background steering (BS) cube, which contains the overall dip trends of the seismic reflectors and outlines the background structural information. This steering cube is taken as input for data enhancement by filtering.

4.1.2. Filtering the data

The seismic volume (SV) is filtered using the dip-steered median filter (DSMF). The key objective behind this filtering is to differentiate between the dip-azimuth of seismic reflections and the overlying noise (Chopra and Marfurt, 2007), remove random noise and enhance the lateral continuity of the seismic events (Hocker and Fehmers, 2002; Kumar and Mandal, 2017; Kumar and Sain, 2018). The DSMF is a statistical filter that is applied on seismic data volume using the pre-processed steering cube (see "Section 4.1.1") for obtaining a smoothed seismic volume where the continuity of seismic reflections is improved by suppressing background random noise (Jaglan et al., 2015). The filter applies median statistics over seismic amplitudes following the seismic dips. This is performed using a 3 × 3 median filtering step-out. The output at this stage is the DSMF seismic data. This conditioned data along with the detailed steering cube then act as primary inputs for attribute extraction followed by designing of artificial neural network (ANN) architecture and validating the output.

4.2. Seismic expressions of buried geologic structures: key to attribute extraction

Once the seismic data is conditioned, we move to search for seismic expressions of geologic features (e.g., volcanoes, sills, dykes, etc.) belonging to the buried system from the data such that an initial hint regarding their structural characteristics (e.g., orientation, shape, extension) are apprehended. These characteristics help in selecting suitable seismic attributes (SA) to be extracted from the data. Volcanoes have a tendency to pierce vertically through the host sedimentary succession. Internally, they are associated with distorted and chaotic reflections and dissimilar seismic events. Over the crater and along the flanks they are associated with high amplitudes due to larger impedance contrast with the surrounding sedimentary rocks (Infante-Paez and Marfurt, 2017; Bischoff et al., 2017). While piercing through the host geologic formations, these features tend to possess variable dips. Seismic energy, when passed through these features, becomes diminished. The flanks and the crater of the volcano are linked with high coherent energy. Sills and dykes generally act as conducive pathways for the movement of magma into the overlying sedimentary units. Sills are concordant intrusive bodies, commonly sub-horizontal with a gentle inclination cross-cutting the subsurface stratigraphy and exhibit major impact on basin history and petroleum system (Smallwood and Maresh, 2002; Thomson and Hutton, 2004; Cartwright and Hansen, 2006). On seismic section, these appear as saucer shaped, gently inclined, distinctly high amplitude and discontinuous in nature. However, dykes vertically intrude into the overlying younger strata and exhibit steep dips.

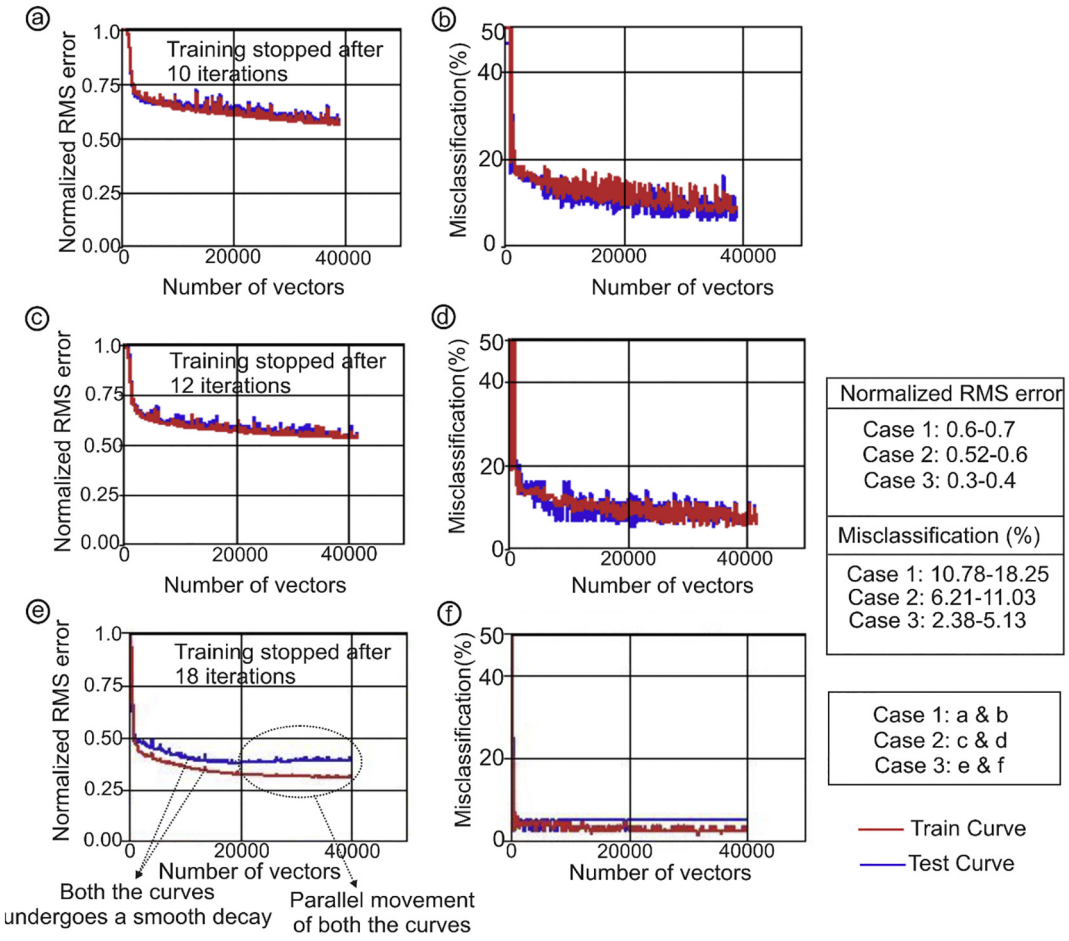

Fig. 7. Normalized RMS error (a) and Misclassification percentage (b) for training (red) and testing (blue) data for Case I; Normalized RMS error (c) and Misclassification percentage (d) for training (red) and testing (blue) data for Case II; and Normalized RMS error (e) Misclassification percentage (f) for training (red) and testing (blue) data for Case III. (For interpretation of the references to colour in this figure legend, the reader is referred to the web version of this article.)

Table 3
Sensitivity chart showing the relative contribution offered by each individual attribute for neural training in Case I.

Attributes	Weights
Dip Magnitude	97.2
Coherency (MW)	94.8
Energy (MW)	92.1
Reference Time	84.5
Curvature (MP)	81.9
Signal to Noise (s/n)	78.5
Energy (SW)	62.5
Coherency (SW)	58.7
Azimuth (MW)	52.7

LW: Long window; SW: Short window; MW: Mid window; MP: Most Positive.

4.3. Attribute selection: preparation of test data sets

Being conceived with the seismic expressions of the geologic features of the buried system, we select a set of attributes that tend to capture their maximum geological responses from the data (Meldahl et al., 2002; Aminzadeh and de Groot, 2006; Kumar and Sain, 2018). For this, we divided the set of attributes into three different cases (I, II and III). The purpose of dividing the attributes into three different cases is to ascertain an optimum or best possible case that can capture the extension and distribution and prominently showcase the plumbing system (consisting of sill networks, dyke swarms, ascent of magma and its emplacement) for realistic interpretation. The Case I consists of a set of attributes e.g., coherency, energy, dip magnitude, azimuth and curvature, which have been documented to be very effective in interpreting igneous bodies from seismic data (Chopra and Marfurt, 2007; Pena et al., 2009; Zhang et al., 2011). The Case II belonging to a set of attributes (a bit different from Case I) consists of energy, dip angle variance, similarity, envelope and energy gradient. The Case III includes energy, dip angle variance, similarity and envelope. The reference time and signal/noise (S/N) ratio are common to all cases. Attributes belonging to these three cases are parameterized at different step-outs and windows. Large, medium and short vertical time windows (e.g., 160 ms, 100 ms, 80 ms, 64 ms and 24 ms) (Table 1) are used for designing the attribute such that the entire geological responses (extension and distribution) of the targets are efficiently captured. The coherency mid-window, coherency short-window, energy mid-window, energy short-window, dip magnitude, azimuth and most positive curvature attributes have been used for Case I. Whereas, the dip angle variance short-window, dip angle variance long-window, energy short-window, energy mid-window, energy long-window, steered similarity, envelope and energy gradient attributes are used in Case II. The Case III uses the dip angle variance short-window, dip angle variance long-window, energy short-window, energy mid-window, energy long-window, steered similarity and envelope attributes.

Table 4
Sensitivity chart showing the relative contribution offered by each individual attribute for neural training in Case II.

Attributes	Weights
Dip Angle Variance (SW)	98.5
Reference Time	83.5
Signal to Noise (s/n)	78.5
Steered Similarity	77.8
Dip Angle Variance (LW)	75.0
Envelope	73.2
Energy (SW)	72.1
Energy (LW)	68.2
Energy (MW)	58.5
Energy Gradient	42.4

LW: Long window; SW: Short window; MW: Mid window.

4.4. Training locations: preparation of trained data sets

After extracting suitable attribute(s) from the data volume, we then move to aggregate these responses and train them over suitable example locations picked from the data. The example locations are broadly classified into two different classes, e.g., object and non-object classes (Aminzadeh and de Groot, 2006). The object classes are the set of all possible locations for the presence of intrusion, whereas the non-object classes are all other locations without any signature of subsurface disturbances caused by intrusion. Around 1650 example locations are picked from each seismic line of the data volume. The training locations are the same for all cases (Case I, II and III).

4.5. Network design

The neural network chosen for designing the meta-attribute is a fully connected multi-layer perceptron (MLP) network (Meldahl et al., 2002; Aminzadeh and de Groot, 2006; Kumar and Sain, 2018). The perceptrons are organized into layers. In its simplest form, the MLP consists of three distinct layers: the input layer, the hidden layer and the output layer. The data fed into the neural network moves from the input layer, gets processed in the hidden layer and are extracted in the output layer. Allocating the number of neurons in the hidden layer is pivotal, as it controls the overall structure of the network and also has significant influence on the final result (Cybenko, 1989; Hornik, 1991; Hinton et al., 2006). Moreover, use of too many neurons in the hidden layer increases the time to train the network and often encounter problems such as overfitting. Hence, many authors (Hornik, 1991; Hinton et al., 2006; Aminzadeh and de Groot, 2006; Singh et al., 2016) prefer less number of neurons in the hidden layer. This would ultimately enhance the processing speed resulting into a smooth performance of the network. Each of the neurons within the network is interconnected through synaptic weights that strengthen the connection. An activation function is used to rescale the neural output (Singh et al., 2016; Kumar and Mandal, 2017; Kumar and Sain, 2018). In the present study, the MLP network uses a sigmoid function that is continuous, monotonically increasing, differentiable, bounded and takes the input and squashes the output in terms of 0 s and 1 s where, 0 refers to intrusion 'no' and 1 refers to intrusion 'yes'. For Case I, the input, hidden and output layers consist of 9, 5 and 2 interconnected nodes. For Case II, the input, hidden and output layers consist of 10, 5 and 2 interconnected nodes. For Case III, the input, hidden and output layers consist of 9, 5 and 2 interconnected nodes. Other network parameters e.g., learning rate and momentum helps in controlling the amount of change required to be incorporated into the connection links or weights between the input, hidden and output layers. Learning rate and momentum values are very often assigned to the network in a trial and error basis (Poulton, 2001). In the present study, the learning rate and momentum for all the three cases are tuned to 0.01 and 0.25 respectively (Table 2). Such small value of learning rate though would slow down the convergence rate of the network, but would help in ensuring that global minimum is not missed. A constant bias (node or threshold) of 1.0 is fed into the

Table 5
Sensitivity chart showing the relative contribution offered by each individual attribute for neural training in Case III.

Attributes	Weights
Dip Angle Variance (SW)	99.2
Reference Time	89.5
Envelope	82.4
Signal to Noise (s/n)	80.3
Steered Similarity	74.5
Energy (SW)	73.9
Dip Angle Variance (LW)	70.5
Energy (LW)	68.2
Energy (MW)	62.5

LW: Long window; SW: Short window; MW: Mid window.

network for all of the three cases (Table 2), such that the connection between the input and the processor is maintained and controlled. The network is made to train over the prepared test and train sets. The training begins by randomly splitting the data into train and test sets, in which 30% of the data is used for testing and 70% is used for training. Iterative neural training is performed to establish a minimum normalized root-mean square (nRMS) error between these two data sets (i.e. the train sets, based on interpreter's intelligence and the test sets, extracted from the data) such that a probability output is obtained. The performance evaluation of the neural training is tracked through the normalized RMS (nRMS) error curves and the misclassification percentage (defined in Appendix A & B). The nRMS error curve demonstrates the overall error on the train and test sets, with a scale ranging from 0 to 1, where 0 corresponds to no error and 1 corresponds to maximum error. Both error curve should follow a smooth decay and then continue to move straight. If test curve rises up further, the network encounters an overfitting. Training should be stopped immediately before this happens. A quality control parameter, defined as the misclassification percentage, is used to understand the wrong predictions made during the classification. We follow a general rule of 'the lower/minimum is the nRMS, the lower would be the misclassification percentage'. Once this is achieved, the neural training is stopped and the output is quality checked over key seismic lines. After a satisfactory outcome, the training is carried out over the entire data volume to capture every single disturbance caused by the intruding body within the data volume. This finally generates the IC meta-attributes for three different cases, the output of which is further investigated and validated with the existing geology and other geophysical data set.

4.6. Validation

The minute details of the buried volcanic system, delineated by the newly designed IC meta-attributes, are then matched with the characteristic signatures of geophysical logs from Kora-1 borehole drilled at the flank of the buried volcanic system. For validating the results of such automatic targeted object oriented technique, we use density and resistivity logs of Kora-1A borehole that penetrated the volcanic formation as well as underlying lithological units.

5. Results

5.1. Data enhancement

The subsurface geologic features e.g., the buried volcano and other associated structural elements like sills and dykes are poorly visible in the original seismic volume (Fig. 4a). These features are accompanied with distorted seismic signals and are masked with seismic noise, as evidenced from four compartments (a. I through a. IV). At shallower level (right above the volcanic crater), bright amplitude anomaly (green dotted rectangle) is observed, which are the relicts of volcanic gas chimneys rising upwards. This zone is surrounded with distorted chaotic reflections (light blue dotted oval). The volcanic crater and the flanks of the volcano appear to be heavily masked with distorted and noisy reflections. Sill intrusions (SI) and Dyke swarms (DS) exhibit poor visibility (light blue dotted oval). Moreover, reflections above these features are poor. Reflections within saucer sill complex (SSC) are not continuous and clear. Conditioning the data through DSMF minimizes the

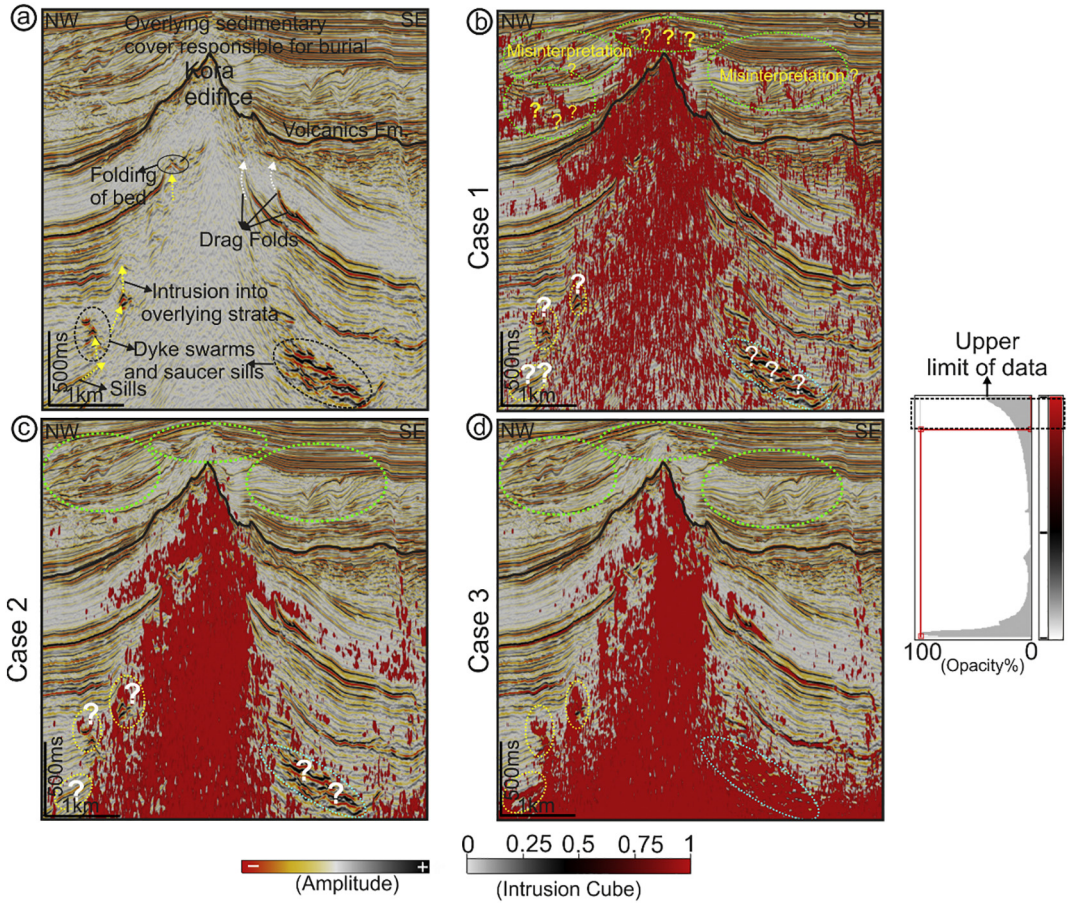

Fig. 8. (a) Interpreted seismic section for inline 1240 displayed with amplitude data; (b) IC meta-attribute for Case I shows image of the buried volcanic system at the cost of some artefacts or misinterpretation outputs; (c) IC meta-attribute for Case II presents the image of buried volcanic complex devoid of any pitfalls but fails to capture the dyke swarms and sill networks; (d) IC meta-attribute for Case III brings out an optimal view of the buried volcanic system along with capturing the geometric distribution of magmatic emplacement bodies. V.E:9.0 is used for all four pannels

masked noise and enhances the lateral continuity of subsurface features (Fig. 4b). The seismic signal within volcanic gas chimney zones, volcanic crater and flanks, sill networks and dyke swarms are improved and free from noisy and distorted reflections, as observed in four compartments (b. I through b. IV). The seismic attributes have efficiently captured the responses of these geological features. A few key seismic attributes (similarity, dip angle variance and energy) that are very important for the interpretation of buried volcanic system is demonstrated in Fig. 5. This has been prepared by co-rendering extracted attribute with the amplitude data. The discontinuous nature of seismic events within the zones at sub-volcanic depth and the Kora edifice (illustrated using white dotted rectangular box) is prominently captured. Faulted structures along the extreme eastern flank of the volcano are illuminated with low similar values (Fig. 5a). The internal zone of the edifice is characterized mostly with high/steep dips (highlighted through white dotted rectangular box) (Fig. 5b). However, the flanks are associated with medium to low dips. Intrusions in the NW part (orange dotted rectangle) possess high dips, medium to low dips are observed for intrusions on the SE part of the section (pink dotted rectangle). The internal zone of the edifice (illustrated through black oval) is associated with low energy (Fig. 5c). The flanks of the edifice are associated with high energy events (green arrows), suggesting large impedance contrast between the igneous materials and surrounding sedimentary rocks. The crest of the volcano is associated with high energy and amplitude events (green arrows). The emplacement movement of magmatic bodies is indicated using orange arrows and their presence is prominently captured by the energy attribute from the surroundings. The responses captured by the similarity, dip angle variance and energy attributes are more appreciated when co-rendered with the amplitude data (Fig. 5d).

5.2. Neural analysis

The extracted attributes for Case I, Case II and Case III are trained over example locations i.e., intrusion yes and intrusion no (Fig. 6a). The 'intrusion-yes' locations are the intrusive elements (dyke swarms and sill networks as illustrated by white dotted ovals and yellow arrows) and internal zones of the Kora edifice. Rest of the host sedimentary units are categorized into 'intrusion-no' locations. The input, hidden and output layers for three cases are demonstrated in Fig. 6b, c and d respectively. The neural training shows a minimum normalized RMS error and minimum misclassification percentage after some iterations (Fig. 7). The normalized RMS error attains a minimum value lying between 0.6 and 0.7 (Fig. 7a) with a minimum misclassification of 10.78% to 18.25% (Fig. 7b) after 10 iterations for Case I. The relative contribution provided by each input set (i.e., seismic attributes) is shown in Table 3, and we observe that the dip magnitude, curvature, coherency and energy (mid-window) deliver the maximum contribution followed by the energy, coherency (short window) and azimuth attributes. For Case II, the normalized RMS error with a minimum value of 0.52–0.60 (Fig. 7c) and minimum misclassification of 6.21% to 11.03% (Fig. 7d) are achieved after 12 iterations. The relative contribution provided by each input set (i.e., seismic attributes) is given in Table 4, which shows that the dip angle variance (short window) and reference time deliver the maximum contribution followed by envelope, steered similarity, signal/noise ratio, dip angle variance (long window) and energy (short, long and mid windows) attributes. The energy gradient attribute exhibits lower contribution. Furthermore, for Case III during the training, we observe that the normalized RMS error attains the minimum value lying between 0.3 and 0.4 (Fig. 7e) with a minimum misclassification of 2.38% to 5.13% (Fig. 7f) after 18 iterations. The training curves, compared to Case I and Case II, exhibit a smooth decay pattern. The relative contribution provided by each input set (i.e., seismic attributes) shows that the dip angle variance (short window), reference time, envelope and signal/noise ratio offers the maximum contribution followed by energy (short, long and mid windows), dip angle variance (long window) and steered similarity (Table 5).

The extracted output for each case is now investigated by co-rending with the amplitude from the same seismic data (Fig. 8a) to collude for an optimum meta-attribute to best represent the extension and distribution of buried volcanic system. Different elements of the buried volcanic system e.g., sill networks, dyke swarms, volcanic edifice etc., are illustrated in Fig. 8a. Emplacements of these structural elements into the host sedimentary units modulated the subsurface structural architecture resulting into jacking up sedimentary strata, drag folds etc. The top of the volcanic formation is marked with black solid line. It is observed that the meta-attribute for Case I brings out several artefacts or misinterpretation outputs (green dotted oval with yellow question mark, Fig. 8b) that are against the regional geology of the prospect. Most of the portions above the top of the volcanic interval are linked with high IC values, suggesting further extension of the buried volcano. By comparing this with the regional geology (Figs.8a and 2b), it is observed that the sequence above the volcanic interval is a thick sedimentary cover of the Giant Foreset that have buried the volcanic complex. Towards the deeper part of the section, we see that the IC meta-attribute for Case I fails to capture the intruding elements e.g., dyke swarms and sills (yellow and blue dotted oval with white question mark, Fig. 8b). The meta-attribute for Case II (Fig. 8c) efficiently images the buried subsurface system and honors the regional geology of the prospect. The shallower parts representing the thick sedimentary cover are devoid of artefacts. However, the IC meta-attribute fails to capture the geometrical shape and orientation of dyke swarms and sills in deeper section (yellow and blue dotted ovals with white

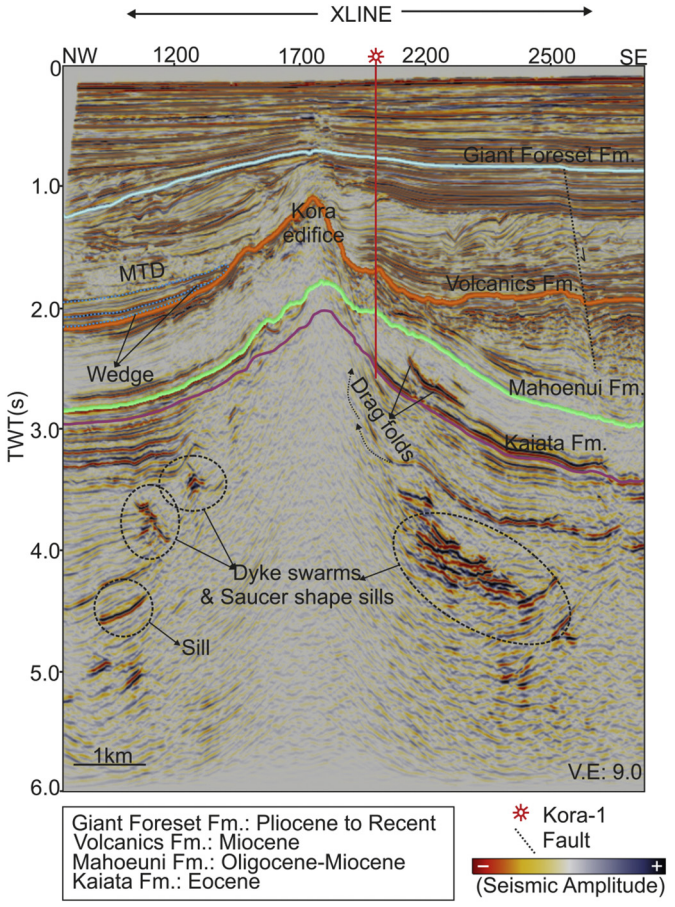

Fig. 9. Interpreted seismic section for inline 1240 displayed with amplitude data. The Kora-I well is shown by solid red line. Top of different geologic formations are marked. Intrusions into the host sedimentary units bring out changes in the subsurface structural architecture (causing jacking up of the sedimentary strata). The drilled well penetrates the volcanic formation through the flanks of the Kora edifice. (For interpretation of the references to colour in this figure legend, the reader is referred to the web version of this article.)

question mark, Fig. 8c). The meta-attribute for Case III (Fig. 8d) enlightens the extension and distribution of buried volcanic system along with other structural elements such as the dyke swarms and sills. These elements emplace magmatic material into the overlying sedimentary strata affecting the structural architecture. The IC meta-attribute captures these events in the deeper part demarcating the vertical nature of intrusion. The geometric shapes of the saucer, steep/gentle dipping features are effectively captured by this IC-meta attribute. The lateral extension of the buried volcano is highlighted. The shallower part with thick sedimentary cover are now devoid of any artefacts, as was earlier imaged by IC meta-attribute for Case-I. The IC meta-attribute volume based on Case III has brought out an optimum and reliable picture of the subsurface from 3D time migrated seismic data for further interpretation and discussion.

5.3. Geologic interpretation using IC meta-attribute

The Kora volcano confined by the sedimentary strata is shaped with three different stratigraphic setups e.g., premagmatic, synmagmatic and postmagmatic events. The premagmatic sedimentary intervals belonging to the Paleocene through Eocene to Oligocene periods (Bischoff et al., 2017) are not deformed by the magmatic processes. The synmagmatic sequence consists of synintrusive, syneruptive and intereruptive events. The synintrusive events are linked with magmatic intrusions (sills, dyke swarms, plumbing of magma) and responsible for modulating the structural architecture of overlying sedimentary strata (Fig. 9). The intereruptive events are related to sedimentary deposits formed during the volcanic quiescence period. The postmagmatic sequence is shaped with burial processes of the volcanic edifice after volcanism ceased (Fig. 9). Here, we attempt mainly to shed light on the usage of IC meta-attribute for interpretation of synmagmatic events of the buried volcanic complex. Interpretations for the pre and post magmatic events are not discussed much. The synmagmatic sequence of the buried volcanic system consists of a complex plumbing system that includes saucer shape sills, dyke swarms, and magma chambers. The structural elements are mostly observed in the deeper part of the seismic section (2.0 to 5.0 s two-way-travel time) (Figs. 9 and 10). The sills in the NW and SE part demonstrate saucer shape patterns (Figs. 10a, c & e) and exhibit concave-upwards cross sectional architecture. Moreover, sills in the SE part exhibit broken bridge and stepped geometries. The vertically intruding dyke swarms restrict their appearance in the NW part only. It is observed that the sills in isolation (NW part, Fig. 10a) cause little deformation to the overlying sedimentary strata. The host sedimentary units are intruded by sill networks and dyke swarms (white dotted oval in the deeper part). The flanks of the Kora edifice are faulted and several radial faults are observed to diverge out from the center of the edifice. Ascent of magma (AOM) (white dotted arrow) is observed at sub-volcanic depth of the Kora edifice. The change in the structural architecture of the overlying sedimentary formations is clearly observed at the NW part (Fig. 10c). Movements of intrusive elements (dyke swarms and saucer sills, as indicated by yellow and white dotted ovals) into the host sedimentary units are shown by

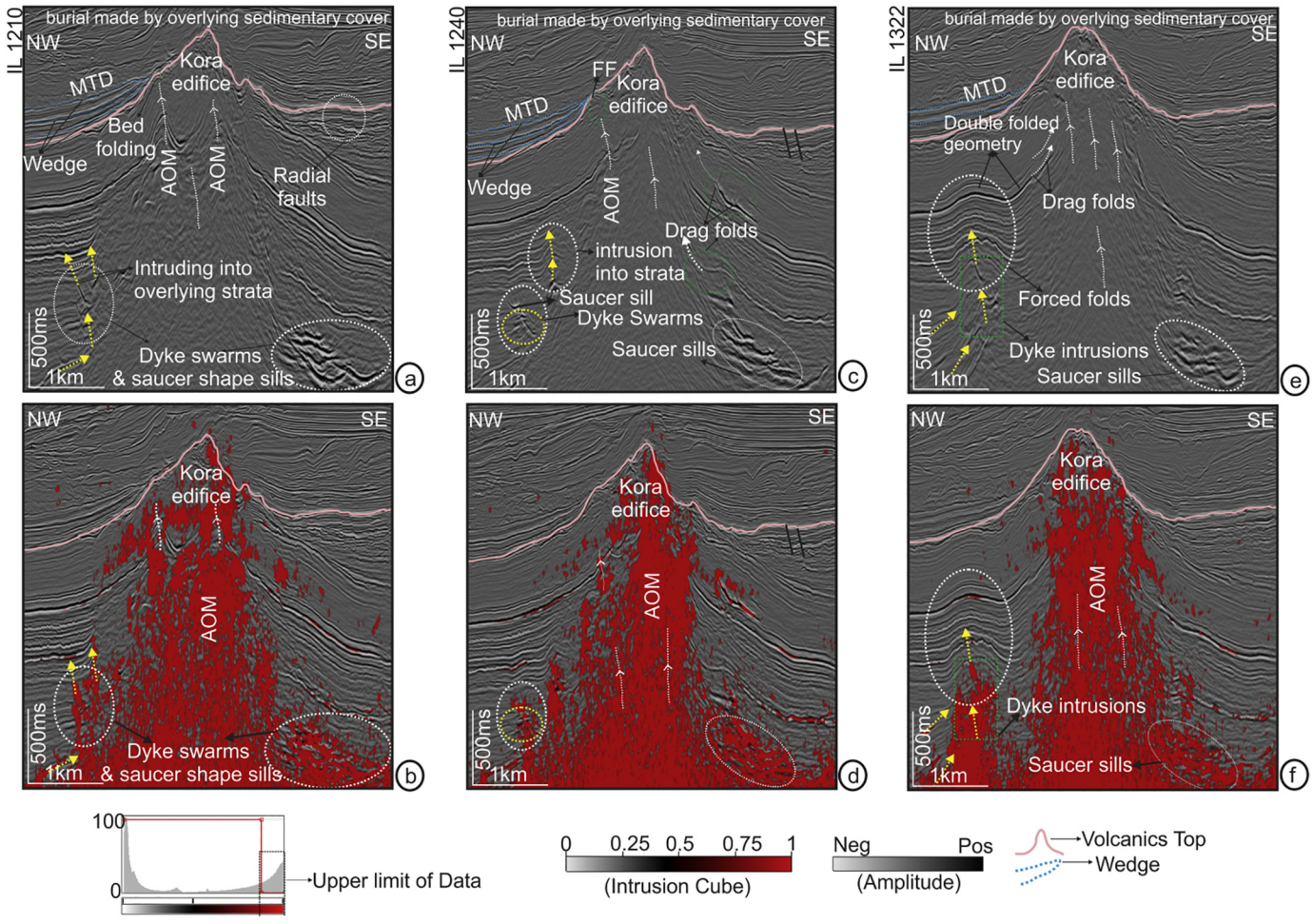

Fig. 10. (a) Interpreted seismic section for inline 1210 displayed with amplitude data. The top of the Kora edifice is shown by solid cream lime; (b) The IC meta-attribute co-rendered with amplitude data for inline 1210 distinctly shows the activities; (c) Interpreted seismic section for inline 1240 displayed with the amplitude data; (d) The IC meta-attribute co-rendered with amplitude data for inline 1240 clearly illuminates the activities; (e) Interpreted seismic section for inline 1322 displayed with the amplitude data; (f) The IC meta-attribute co-rendered with amplitude data for inline 1322 conspicuously brings out the extension and distribution of the buried volcanic system. V.E:9.0 is used for all 6 pannels

yellow arrows. Drag folds (green dotted oval and white dotted arrows) that have resulted from magmatic emplacement into the sedimentary strata are also observed. The complex plumbing system is observed beneath the volcanic edifice (Figs. 10a, c and e), which possess discontinuous character and crosscuts sedimentary unit below the volcanic interval.

The magmatic emplacement into the host sedimentary interval (or the premagmatic sequence) cause large structural deformation and most of these activities are overserved in the sub-volcanic depth of 2.5 to 3.5 s two-way-travel time (Figs. 9 and 10). Emplacement to the sedimentary formations has resulted into the development of forced folds exhibiting double folded geometry (Fig. 10e). These structures are tilted away from the primary vent of the Kora edifice. The IC meta-attribute (Figs. 10b, d and f) attempts to capture these findings and brings out robust visualization of these processes. The geometrical architecture of saucer shape sills and vertically intruding dyke swarms are clearly imaged by the IC meta-attribute. These structures are associated with high IC values. Interpreted magmatic plumbing system and pathways of magmatic emplacement within the sedimentary intervals is prominently demarcated by the IC meta-attribute (Figs. 10b, d and f). The Kora edifice, associated with high values of IC meta-attribute, brings out the vertical and lateral extension of the volcano.

Dyke swarms and sills act as prominent structures for emplacing magma into the overlying sedimentary units. This has resulted into forced folds, double folded geometry pattern, drag folds, observed in NW (white dotted ovals & black arrows) part of the study area. These observations are illustrated through green rectangular box and white dotted oval and movements of magmatic fluids are demarcated through yellow arrows (Figs. 10a-f). The IC meta-attribute has prominently captured these events within the study area. This is better understood from a time slice $t = 2.7$ s, viewed with energy gradient attribute (Fig. 11a). The IC meta-attribute, co-rendered with the energy gradient attribute, demonstrates high IC values within the Kora edifice and nearby forced folds (Fig. 11b). A random line AB confirms these observations, where dykes are perceived to intrude into the overlying sedimentary units (green dotted arrow and white dotted oval) causing double folded geometry of geological beds (yellow dotted oval) (Fig. 11c). The IC meta-attribute, co-rendered with the amplitude data, highlights all these facts (Fig. 11d). Furthermore, a time slice $t = 4.2$ s demonstrates the structural geometry of sill complex and dyke swarms (Fig. 12a). The energy gradient attribute, co-rendered with the IC meta-attribute for the same time slice, shows high IC values within the volcanic core, sill complex, dykes and the surrounding areas (Fig. 12b). The sill complex and dyke swarms are distributed in the eastern and western part of the buried volcanic complex. Random lines CD and EF illustrate their geometric nature and structural presence. Sills within the sill complex are interconnected and possess broken bridge geometrical pattern (Thomson and Hutton, 2004) and saucer shapes (Fig. 12c). The dyke swarms tend to vertically intrude into the overlying-sedimentary units. Such intrusions emplace magma into these formations thereby causing dome and folded geometry of the overlying beds (Fig. 12d). Magmatic ascent into shallow sedimentary intervals at the flanks of the Kora edifice results into forced fold dome. This is clearly observed from the co-rendered plot of dip angle, azimuth and IC attributes over time

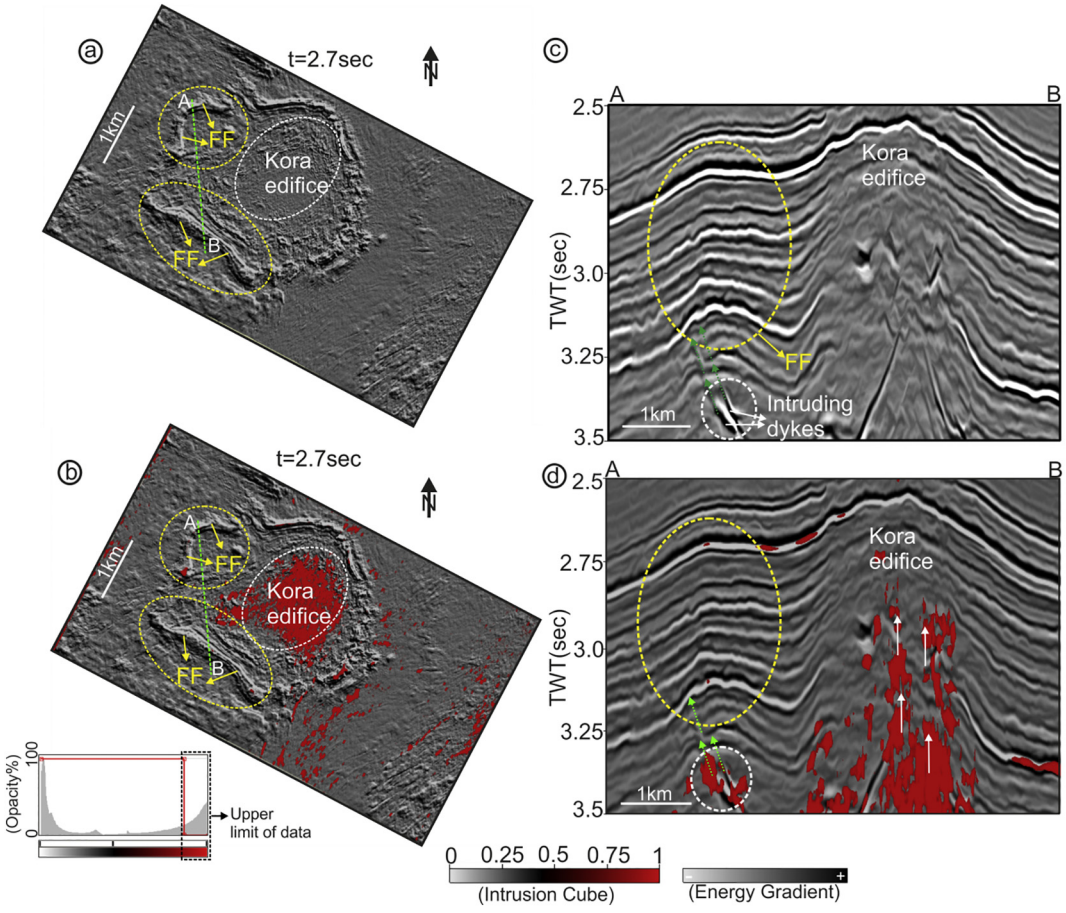

Fig. 11. (a) Time slice at $t = 2.7$ s, displayed with energy gradient attribute, brings out structural view of the Kora edifice (white dotted oval) and associated domed strata like the forced folds (FF) (yellow dotted oval); (b) The energy gradient attribute, co-rendered with the IC meta-attribute, for the same time slice. High IC values are observed within the Kora edifice, surrounding areas and zones near FF; (c) Random line AB, shows the relevance of these observations; (d) The amplitude data, co-rendered with the IC meta-attribute, for the same random line shows high IC values within the zone of magmatic emplacements. (For interpretation of the references to colour in this figure legend, the reader is referred to the web version of this article.)

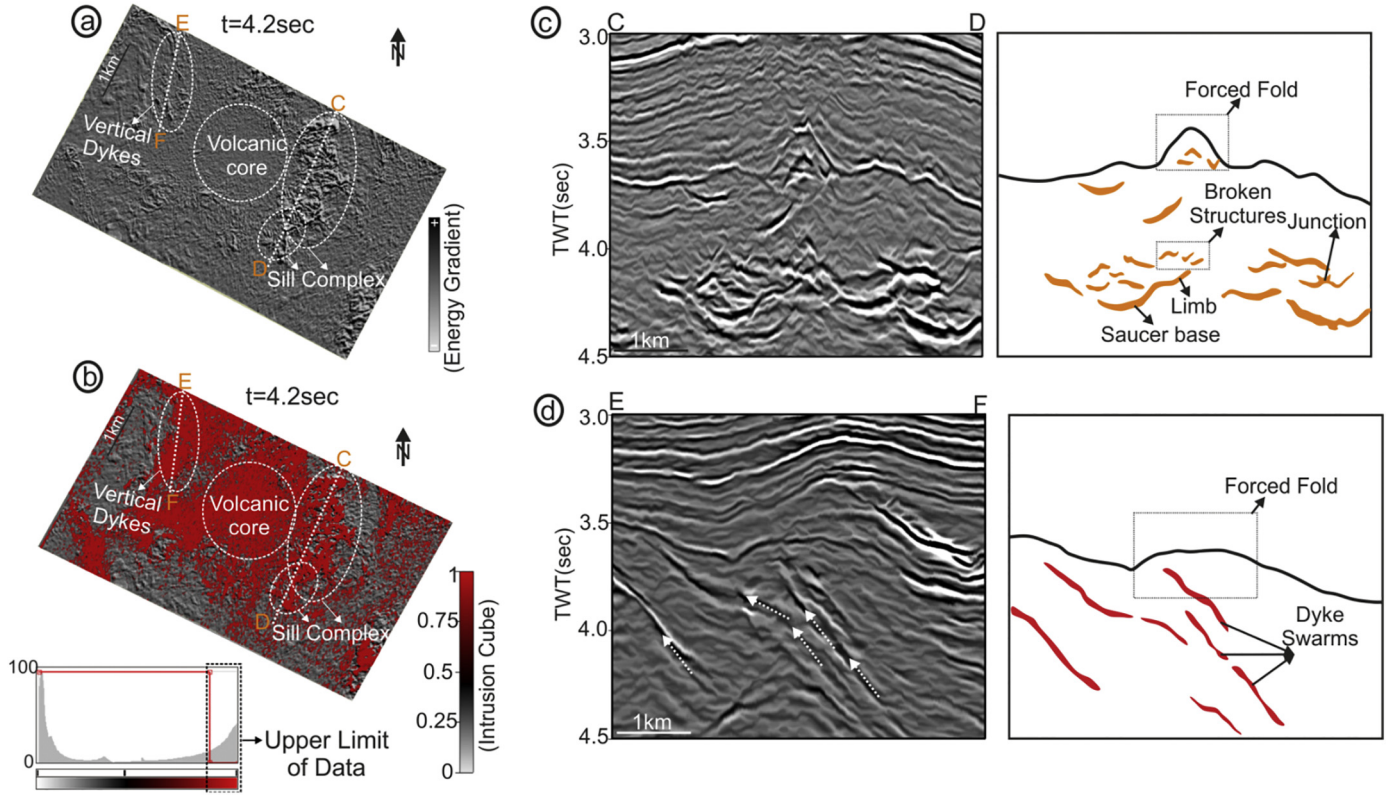

Fig. 12. (a) Time slice $t = 4.2$ s displayed with energy gradient attribute brings out the structural view of the saucer shape sill complex and dyke swarms (white dotted ovals). The volcanic core is indicated by white dotted circle; (b) The energy gradient attribute, co-rendered with the IC meta-attribute for the same time slice; (c) Random line CD highlights the relevance of sill networks. The sills exhibit saucer shape and broken bridge patterns; (d) Random line EF highlights the presence of vertically intruding dykes (marked with white dotted arrows).

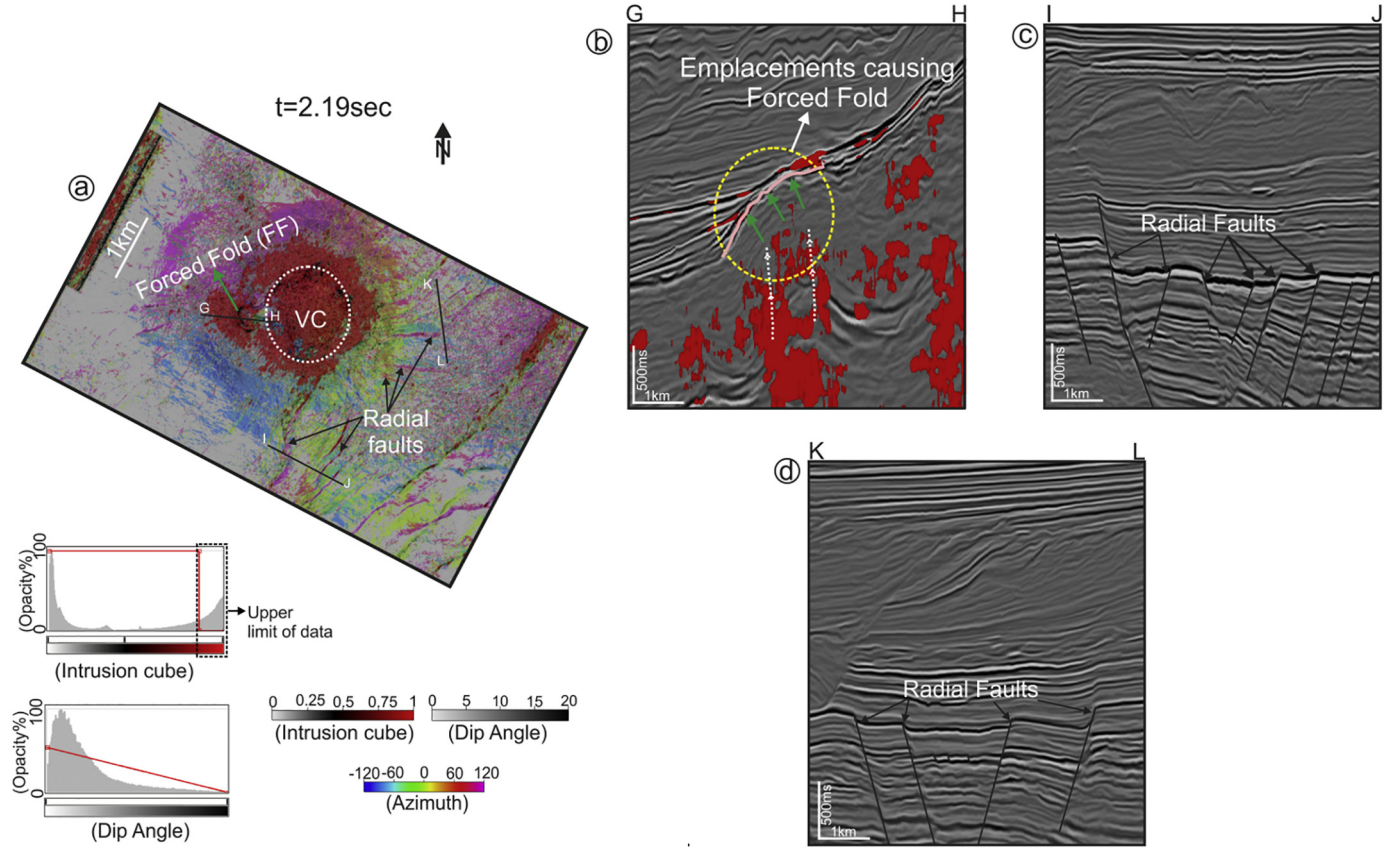

Fig. 13. (a) Time slice at $t = 2.19$ s displayed with co-rendered attributes such as azimuth, dip magnitude and IC meta-attribute. (b) Random line GH, perpendicular to such deformation, shows magmatic emplacements (white dotted arrow) into the volcanic edifice resulting into doming of the flanks creating forced folds (FF) (yellow dotted oval and green arrows). The domed portion is indicated through solid cream line; (c)-(d) Radial faults diverging out from the volcanic crater are highlighted through random lines IJ and KL. (For interpretation of the references to colour in this figure legend, the reader is referred to the web version of this article.)

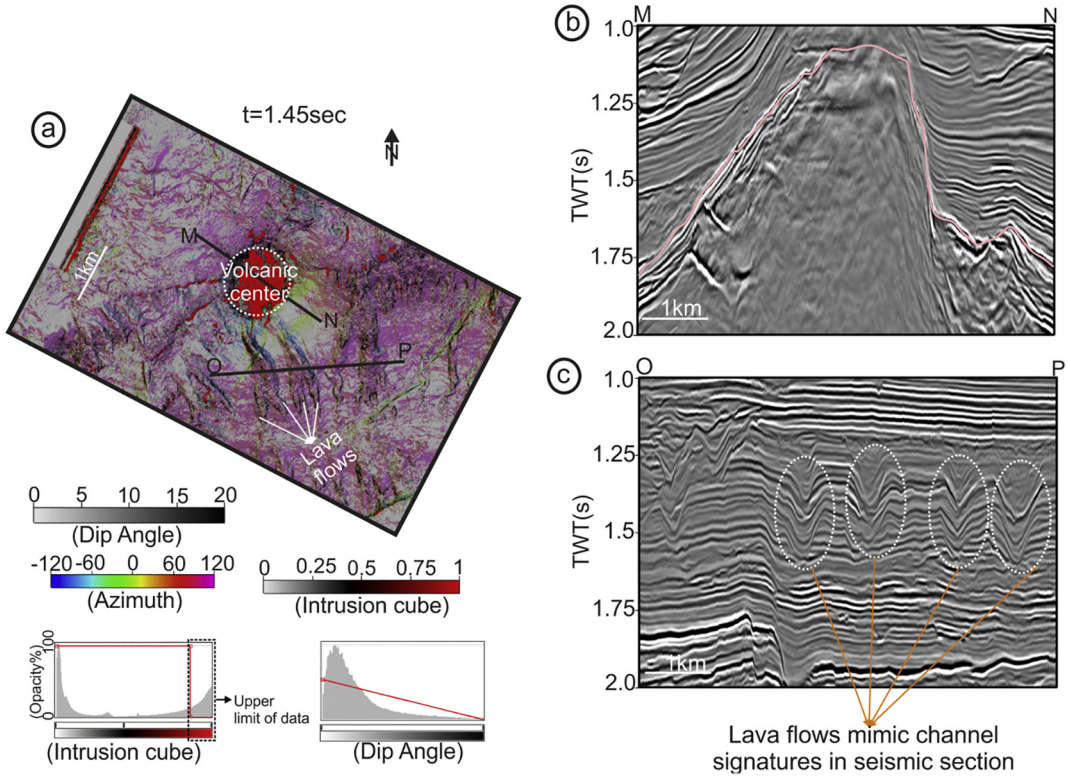

Fig. 14. (a) Time slice $t = 1.45$ s displayed with co-rendered attributes (azimuth, dip magnitude and IC meta-attribute). (b) Random line MN, perpendicular to the volcanic edifice and displayed with the amplitude data, shows the Kora edifice (cream solid line); (c) Random line OP, perpendicular to the lava flows and displayed using amplitude data, mimics channel signatures in seismic section.

slice $t = 2.19$ s two-way travel time (Fig. 13a). This forced dome structure is linked with several radial faults (black arrows) that diverge out from the volcanic core (white dotted circle). Forced folds (FF) (green arrow) are observed closer to the flanks of the Kora edifice. A random line GH, prepared perpendicular to this domed structure and viewed through a co-rendered display of the IC meta-attribute and amplitude data, shows the reliability of above observations (Fig. 13b). Moreover, the random lines IJ and KL bring out the presence of radial faults that

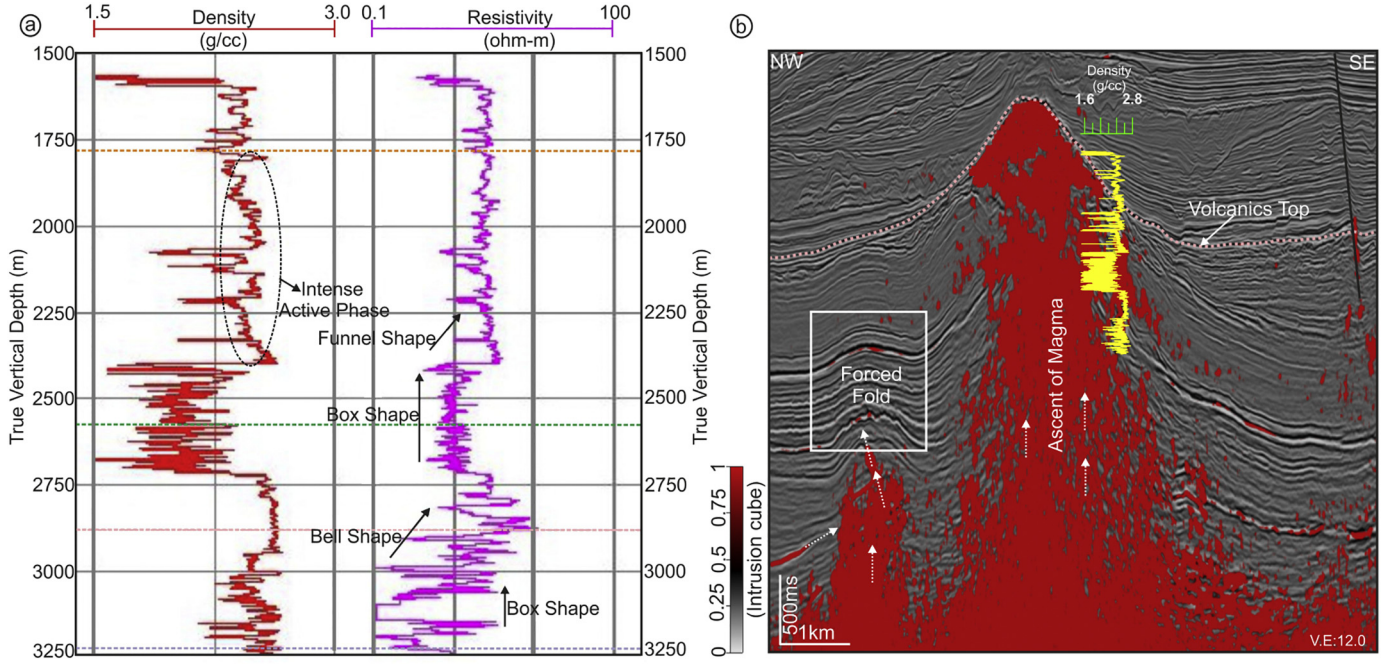

Fig. 15. (a) Density log (red) and resistivity log (pink) in the Kora-1 borehole drilled within the prospect. Different stratigraphic horizons are marked (violet dotted line for Kaiata Fm.; pink dotted line for TeKuiti Fm.; green dotted line for Mohoeneui Fm.; orange dotted line for Volcanic Fm.). The volcanic formation that remained active during the Miocene period is associated with high density and high resistivity; (b) Seismic section, co rendered with meta-attribute and superimposed with density log data, showing different elements along with the ascent of magma. (For interpretation of the references to colour in this figure legend, the reader is referred to the web version of this article.)

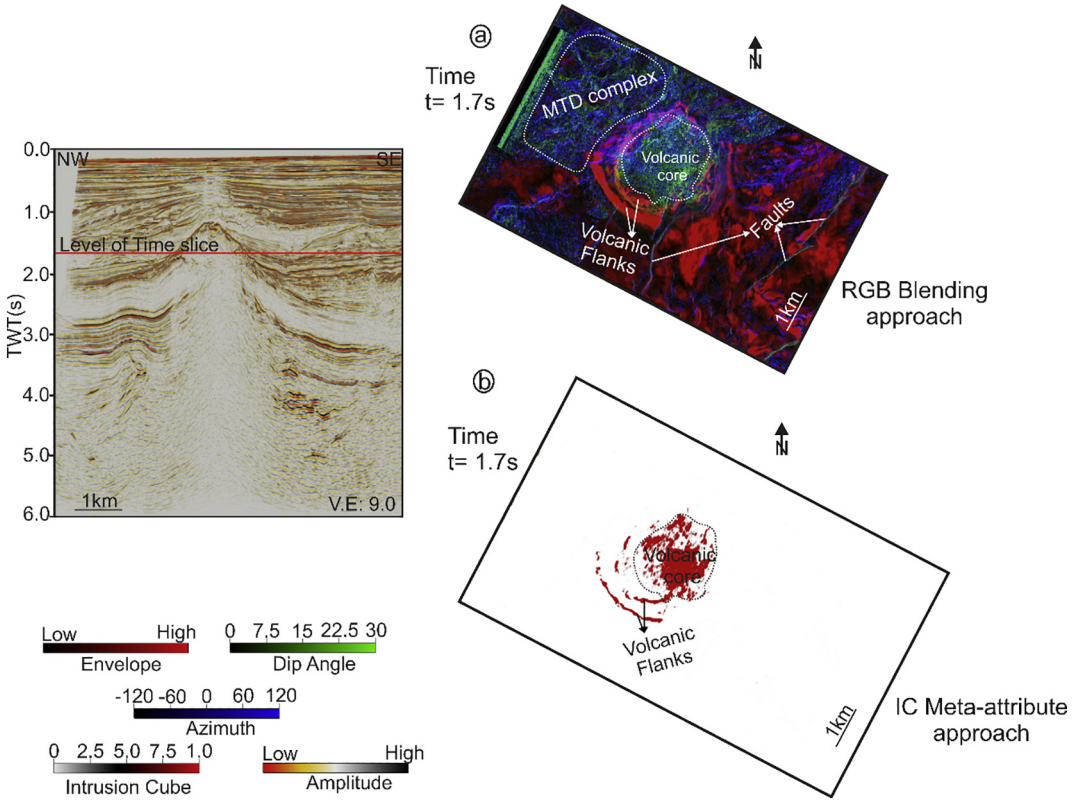

Fig. 16. (a) Time slice at $t = 1.7$ s displayed with RGB volume blending of amplitude envelope, dip angle and azimuth attributes. The image brings out a mixed set of geologic features that includes the volcanic complex, MTD and discontinuous features; (b) Time slice at t = 1.7 s displayed with the IC meta-attribute reveals the geologic target of interest i.e., the volcanic complex.

diverge out from the volcanic crater (Figs. 13c and d). The syneruptive elements of the synmagmatic sequence include zones surrounding the volcanic cone. These zones are confined to a depth of 1.3 to 2.4 s two-way travel time (Fig. 9). It consists of main vent complex of the Kora edifice and eruption related deposits. The top of the main vent complex and the flanks are associated with high amplitude, and is characterized with an amalgamation of coherent and disrupted reflections that diverge out radially from the center (Fig. 9 and Figs. 14a and b). The volcanic core is associated with high IC values (Fig. 14a). The lava flows are observed to diverge along the flanks from the center of the volcanic edifice. The IC-meta attribute illuminates the main vent complex of the Kora edifice, visualized both in plan-view (Fig. 10) and map-view (Fig. 14a). The random line MN drawn perpendicular to the volcanic center illuminates the Kora edifice (Fig. 14b). The deposits of lava flow mimic the channelized geometry pattern and diverge out radially from the center of the eruptive vent (Fig. 14a). It is observed that the thickness of these deposits varies between 34.92 and 44.63 m for an assumed interval velocity of 5500 m/s (Skogly, 1998). The eruptive deposits decent along the flanks from the center, gets channelized and bifurcated to produce large lobate deposits. Random line OP is drawn perpendicular to their flow direction to confirm their channelized appearance both in map and plan views (Figs. 14a and c).

The intereruptive elements of the Kora volcanic system include deposits formed due to the interaction of volcanic eruption and non-volcanogenic sediments. Lithofacies derived from the drilled Kora wells suggest that the synmagmatic sequence consists of intercalation of sedimentary and eruptive deposits (Bergman et al., 1992; Bischoff et al., 2017) which are the product of the syneruptive and intereruptive intervals. Bischoff et al. (2017) documents a detailed view of core (photographs and descriptions) derived from the drilled well Kora-1. The IC meta-attribute primarily aims to capture the structural architecture of the buried volcanic system. However, mapping of volcanic lithofacies is not the objective of the present research. In this regard, Infante-Paez and Marfurt (2017) have brought out a detailed description of volcanic facies developed within the Kora volcanic system. The postmagmatic sequence consists of the degradation and burial process of the Kora edifice that underlies the entire synmagmatic strata. Towards the SE part of the Kora volcanic system, the geological strata deposited during the degradation process is well preserved and is marked by downlap reflections along the flanks of the volcano (Fig. 9). In the NW part of the Kora volcanic system, the deposited degradational sequence is deformed by mass transport deposits (MTDs) developed due to seafloor collapses. The MTDs occurs at a depth of 1.6 to 1.9 s two-way travel time and is associated with chaotic and disrupted seismic reflections (Fig. 9). The transport direction of MTDs was from SE to NW (Bischoff et al., 2017) and this could be linked for the construction of slope and basin morphology during the Pliocene progradation. The overlying Giant Foreset formation containing progradation of clinoforms from SE to NW marks the upper limit of the degradational stage of the Kora edifice (Fig. 9), which was buried in the slope to shelf environment (Bergman et al., 1992; King and Thrasher, 1996; Hansen and Kamp, 2008). The base of the burial stage is marked by the prograding clinoforms from SE to NW during the Late Neogene regression. The Kora edifice was covered with the overlying sedimentary formations, the activity of which continued for millions of years leading to the complete burial of the volcanic system.

Table 6
Computation time for individual attributes in volume blending (VB) process and the multi-layer perceptron (MLP) neural training. The MLP neural model involves a combination of several other attributes as shown in Table 5.

Individual attributes for VB and the MLP neural model	Computation Time (in seconds)
Amplitude Envelope	2679
Dip Angle	6329
Azimuth	8647
MLP neural model for Case III	17

5.4. Validation of the IC meta-attribute

The inferences drawn using the IC meta-attribute are validated through the log signatures of the Kora-1 exploratory well, which was drilled within the prospect by ARCO Petroleum to verify the presence of Eocene Tangora sandstone units within a large dome structure associated with the Miocene volcanics. The well was drilled up to a depth of 3241 m and is reported to encounter hydrocarbons at the top of the Miocene volcanics and upper and lower Tangora sandstone units. Production test within the Miocene volcanic section delivered 1168 bopd (ARCO, 1988). We use the density and resistivity logs (Fig. 15a) to validate the IC meta-attribute computed along a seismic line (Fig. 15b) passing through the borehole. The borehole penetrated through Miocene (Volcanics formation; 1781.2 m), the Oligocene (TeKuiti formation; 2898.5 m), the Oligocene-Miocene (Mohoeneui formation; 2581.5 m) and terminated at the end of the Eocene (Kaiata formation; 3241.8 m). The zone lying between ~1781 m to 2375 m depth was prone to severe igneous activities throughout the entire Miocene period, as observed by high density and high resistivity in the logs. The superposition of logs over the seismic section indicates this phenomenon. The depth interval between ~2375 m to 2750 m, associated with low density and low resistivity, suggest that though magmatic activity took place but was not so severe during the Eocene-Oligocene period. However, relicts of these activities comprising plumbing system, magmatic feeder, ascent of magma etc. prevailed within these periods which are highlighted by the IC meta-attribute. The zones between ~2750 m to 3241 m accompanied by high density and high resistivity and further below are associated with high IC. Such a magmatic event that took place over a large geological period from Late Cretaceous through Paleocene, Eocene and Oligocene to Miocene had not only modulated the architecture of the surrounding environment but also generated several structural traps conducive for engulfing hydrocarbon resources.

5.5. IC meta-attribute versus RGB volume blending

To examine the proficiency of the newly designed IC meta-attribute against the RGB volume blending technique (Chaves et al., 2011; Alves et al., 2015; Bischoff et al., 2017), we present a comparison between the RGB volume blending technique and the present IC meta-attribute approach (Fig. 16a-b). Individual attribute volumes e.g., envelope, dip angle and azimuth are blended using red, green and blue colours. We observe that the RGB volume blending approach shows the volcanic complex (volcanic core and flanks) with a mixed set of interpretation that includes MTD complex in the NW and surrounding faulted sedimentary environment (Fig. 16a). Whereas, the IC meta-attribute delivers a focused interpretation that sheds light only on the volcanic complex within the data volume (Fig. 16b). This clearly demonstrates the merit of the present approach which intelligently delivers an improved interpretation of geologic target of interest. Moreover, the computation speed of the IC meta-attribute through the proposed MLP approach is much faster (Table 6) than the computation of individual seismic attribute volume through the classic attribute methodology.

6. Discussion

6.1. IC meta-attribute: as a novel automated approach

Interpretation of submarine buried volcanic complexes becomes tiresome when the seismic data is contaminated with coherent and random noises. Their presence degrades the quality of the processed data thereby lowering the S/N ratio (Liu et al., 2006; Onajite, 2014). Thus, advanced data conditioning approaches allow to outwit such problems. The preliminary phase of the present workflow (Fig. 3) aims to improve seismic responses of such complex geological system. The original time migrated 3D seismic data demonstrates that seismic reflections within the buried volcanic system are distorted and prone to noisy events (Fig. 4a. I through IV). These artefacts do not only lead to poor visibility but also hinders steady interpretation. Furthermore, Magee et al. (2015) and Eide et al. (2017) illustrated that the presence of random noise within the data degrades the image quality and reduces the detectability of magmatic features from seismic data. Application of the DSMF to the data resulted into smooth and clean reflections within the buried volcanic system. Conditioning of data volume does not only preserve the structural architecture of the buried system but also improves the signal quality (Fig. 4b. I through IV). The structurally conditioned volume serves as a primary input for extracting attributes and designing ANN to derive the IC meta-attribute. Several authors (Infante-Paez

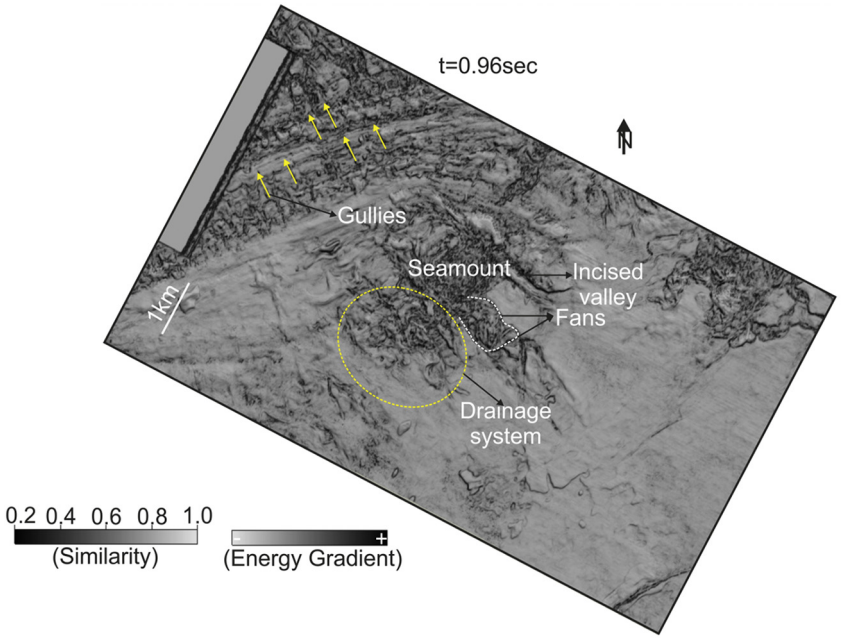

Fig. 17. Time slice at $t = 0.96$ s displayed with co-rendered attributes (similarity and energy gradient). The image of co-rendered attribute brings out several geomorphic features developed during the burial of the Kora edifice, which may be the potential reservoirs for accumulating hydrocarbons.

and Marfurt, 2017; Bischoff et al., 2017) have used high resolution 3D seismic data to effectively interpret the subsurface architecture of the buried volcanic system within the Kora prospect. Bischoff et al. (2017) have used a range of approaches such as attribute analysis, geobodies extraction and volume rendering techniques to reveal different architectural elements of the Kora volcanic system. Infante-Paez and Marfurt (2017) have attempted to interpret lithofacies within the volcanic edifice by using clustering technique like the self-organizing maps (SOM), which is an unsupervised process of learning.

The present study attempts to improve the automatic interpretation strategies of 3D seismic data by exploiting the generalization and abstraction capability of ANNs, with an aim to better image the subsurface and effectively define the tectonic architecture of the buried volcanic system through a new attribute, defined as the IC meta-attribute. Our approach follows a supervised learning scheme in which attributes are extracted from seismic data and trained according to the interpreter's knowledge on targeted objects using state-of-the-art ANN. In this process, seismic attributes are selected depending on the targeted geology such that the maximum information regarding the interpretation targets can be extracted. The IC meta-attribute is different from RGB volume blending approaches (Chaves et al., 2011; Alves et al., 2015; Bischoff et al., 2017), which are non-computer models. We have designed the IC meta-attribute by suitably selecting and parameterizing a set of attributes and the neural network (Tables 1 and 2) so that a comprehensive interpretation of the targeted object can be achieved. For obtaining an optimal set of attributes, we have divided the attributes into Case I, Case II and Case III (Figs. 6b, c and d; Tables 3, 4 and 5), and demonstrated that the IC meta-attribute in Case III is the best suited to capture the extension and distribution of the buried volcanic system including several other intrusive elements such as the sills and dykes etc. (Figs. 8d and 10a–f). We attempt to consistently improve the interpretation strategies such that the misinterpretations and pitfalls regarding geological targets are minimized and a meaningful geological output is generated. The IC meta-attribute obtained from Case III is an optimum answer to such an objective, where the geological targets are effectively illuminated from the seismic data. A scope may lie for further improvement. The IC meta-attribute can be generated in any global environment by different ways from an optimum set of seismic attributes (as showcased in this study). However, it all depends on the geologic objects to be interpreted and the tectonic regime that surrounds them.

6.2. Implications for hydrocarbons and other subsurface resources

Though the study has provided a better interpretation of the buried volcanic systems including the structural elements like the sills and dyke swarms, the regional implications on how such volcanic setting within the sedimentary basin contributes to the generation and preservation of hydrocarbons needs to be addressed. Examples of world-wide volcanic settings that are petroliferous are the Green Tuff formation of Japan, Cabiunas formation offshore Brazil, rhyolites and tuffs of the Qingshen field in China etc. The Kora prospect of the TB also hosts petroliferous magmatic reservoirs (ARCO, 1988), which contain volcanoclastic rocks made up of *syn*- and inter-eruptive deposits. When drilled along the flanks of the Kora volcano, it produced 1168 bopd during Kora-1 well formation test. The principal source rocks of the TB are the Rapoki and North Cape formations of the Pakawau Group (Late Cretaceous to Paleocene). These source rocks contain interbedded coal measures and are made up of Type III kerogene (Stagpoole and Funnell, 2001). The analysis of seismic data suggests for several synintrusive elements e.g., dyke swarms, sill networks etc. (Fig. 9) at depth of 3.5 to 5.0 s two-way travel time. These intrusive elements into the overlying sedimentary succession have modulated their structural architecture. Hatherton et al. (1979) documented that Pakawau Group and overlying sedimentary succession were pierced by several intrusive elements. Allis et al. (1995) further illustrated that such activity resulted in high heat flow and acted as an illuminating tool to mature these source rock units. This suggests that movable hydrocarbons might have been expelled from the Paleocene period into the overlying sedimentary units. The presence of the buried volcanic system has resulted into several hydrocarbon traps and reservoirs to accumulate these hydrocarbon resources. Magmatic emplacement and eruption of the Kora edifice resulted into several synmagmatic traps and reservoirs within the Kora prospect. Structural traps like the forced folds (jacking up the sedimentary strata), drag folds (Fig. 10) are the consequence of intrusive elements e.g., dyke swarms and saucer shape sill networks. These traps have potential to generate closures and accumulate economic volume of hydrocarbon resources (Bischoff et al., 2017). Most of these traps are observed at a depth of 3.5 to 2.0 s two-way travel time in the seismic data. Stratigraphic traps e.g., pinchouts are also observed along the flanks of the Kora volcano (Fig. 10). These traps are tilted upwards in the direction of the Kora edifice and are observed towards the south-eastern part of the volcanic system. The potential reservoirs within the synmagmatic sequence occur in the form of intercalated volcanic and sedimentary deposits and also in the form of fractured igneous rocks (Stagpoole and Funnell, 2001; Bischoff et al., 2017). The proven reservoirs of this sequence include pyroclastic and epiclastic deposits with porosity ranging from 9 to 28% (ARCO, 1988; Bergman et al., 1992; Stagpoole and Funnell, 2001; Bischoff et al., 2017). Several geological traps and reservoirs are also encountered in the postmagmatic sequence of the buried volcanic system. These include paleogeomorphic traps in the form of unconformity, seamounts, valley fills, gullies etc. (Fig. 17) and contribute to the accumulation of hydrocarbon resources. These potential traps are generated during the burial process of the Kora volcanic system (Bergman et al., 1992; Stagpoole and Funnell, 2001) to influence the deposition patterns of sediments through Pliocene to Pleistocene period during which the volcano got buried completely. Potential reservoirs developed due to the degradation and burial of the Kora edifice are seamounts, fans at the edges of the seamounts, dendritic submarine channels, incised valleys, MTDs along the flanks of the edifice etc. (Figs. 17 and 9). The sedimentary deposit of the Giant Foreset formation is composed of well-sorted, fine-grained sand deposits exhibiting an average porosity of ~25% and qualifies to be a good reservoir covering the buried volcanic system (Fletcher Energy Taranaki, 1996).

7. Conclusion

We propose an automated approach based on artificial neural network and design a new attribute, defined as the Intrusion Cube (IC) meta-attribute from a suite of seismic attributes. The meta-attribute has provided a realistic interpretation of geology from time-migrated seismic data in the Taranaki basin off NZ by clearly delimiting the extension and distribution of the subsurface plumbing system. This includes the buried volcano, several intrusive elements such as the sill networks, dyke swarms and magmatic ascent etc. in complex tectonic regime of the Kora field. It is noteworthy to mention that several other new attributes may evolve which could be incorporated into the algorithm to further enhance the interpretation of such a complex magmatic system. This type of interpretational approach is an added contribution to streamline the existing interpretation strategies and unlock newer frontiers of research that aims for rigorous understanding of the subsurface.

Acknowledgement

Thanks are due to dGB Earth Sciences™ for according permission to use their software. The New Zealand Petroleum & Minerals, Ministry of Business, Innovation & Employment, New Zealand Government, are highly acknowledged for providing the seismic and well data. Special thanks are due to the editor-in chief, Dr. Jyoti Behura and five other anonymous reviewers for their critical reviews and fruitful suggestions to improve the quality of work. The first author thanks DST, Govt. of

India for according him with the Inspire Fellowship. There is no conflict of interests among the authors for this submission.

Appendix A. The normalized RMS (nRMS) error is computed from RMS error between the targeted (t_i) and computed (c_i) values for i ranging from 1 to n, which is given as (Aminzadeh and de Groot, 2006)

$$RMS = \sqrt{\frac{1}{n}\sum_{i=1}^{n}(t_i - c_i)^2} \tag{A1}$$

and the,

$$normarlized\ RMS = RMS/\sqrt{\frac{1}{n}\sum_{i=1}^{n}(t_i - mean)^2} \tag{A2}$$

where, the mean is given as:

$$mean = \frac{1}{n}\sum_{i=1}^{n} t_i \tag{A3}$$

Appendix B. The classification accuracy is an important performance controlling parameter used to evaluate the intelligent neural model. To have a good control over this accuracy it is better to create a truly representative distribution of observations in each class. Or else, the classification accuracy could alone be a misleading factor

The classification percentage is defined as the ratio of number of correct predictions to that of the total number of predictions. It is given as:

$$Classification\ (\%) = \frac{Number\ of\ correct\ predictions}{Total\ number\ of\ predictions} \times 100 \tag{B1}$$

The misclassification percentage on the other hand, is defined as the ratio of number of wrong predictions to that of the total predictions. It is given as:

$$Misclassification\ (\%) = \frac{Number\ of\ wrong\ predictions}{Total\ number\ of\ predictions} \times 100 \tag{B2}$$

References

Allis, R.G., Armstrong, P.A., Funnell, R.H., 1995. Implications of high heat flow anomaly around New Plymouth, North Island, New Zealand. N. Z. J. Geol. Geophy. 38, 121–130.

Alves, T.M., Omosanya, K.D., Gowling, P., 2015. Volume rendering of enigmatic high-amplitude anomalies in Southeast Brazil: a workflow to distinguish lithologic features from fluid accumulations. Interpretation 3, A1–A14.

Aminzadeh, F., de Groot, P., 2006. An Introduction to Artificial Neural Networks. Neural Networks and Other Soft Computing Techniques with Applications in the Oil Industry. EAGE Publications, Netherlands, pp. 13–35.

ARCO Petroleum, 1988. Final Well Report, Kora-1 and Kora-1A, PPL 38447. Ministry of Economic Development New Zealand, pp. 1–885 Unpublished Petroleum Report Series, PR 1374.

Barnes, A.E., 2016. Handbook of Post-stack seismic attributes. SEG, Tulsa.

Bergman, S.C., Tablot, J.P., Thompson, P.R., 1992. The Kora Miocene andesite stratovolcano hydrocarbon reservoir, Northern Taranaki basin, New Zealand. New Zealand Oil Exploration Conference Proceedings. Ministry of Economic Development, New Zealand, pp. 178–206.

Bischoff, A.P., Andrew, N., Beggs, M., 2017. Stratigraphy of architectural elements in a buried volcanic system and implications for hydrocarbon exploration. Interpretation 5, SK141–159.

Cartwright, J., Hansen, D.M., 2006. Magma transport through the crust via interconnected sill complexes. Geology 34, 929–932.

Chaves, M.U., Di Marco, L., Kawakami, G., Oliver, F., 2011. Visualization of Geological Features Using Seismic Volume Rendering, RGB Blending and Geobody Extraction. Paper presented at 12th International Congress of the Brazilian Geophysical Society & EXPOGEF, Rio de Janeiro, Brazil (2011), pp. 848–850.

Chopra, S., Marfurt, K.J., 2007. Seismic Attributes for Prospect Identification and Reservoir Characterization. SEG, Tulsa.

Cortez, M.M., Cetale Santos, M.A., 2016. Seismic interpretation, attribute analysis, and illumination study for targets below a volcanic-sedimentary succession, Santos Basin, offshore Brazil. Interpretation 4, SB37–SB50.

Cybenko, G., 1989. Approximation by superpositions of sigmoidal functions. Math. Contrl. Signal. Sys. 2, 303–314.

Eide, C.H., Schofield, N., Lecomte, I., Buckley, S.J., Howell, J.A., 2017. Seismic interpretation of sill complexes in sedimentary basins: implications for the sub-sill imaging problem. J. Geol. Soc. 2017–2096.

Farrimond, P., Bevan, J.C., Bishop, A.N., 1999. Tricyclic terpane maturity parameters: response to heating by an igneous intrusion. Org. Geochem. 30, 1011–1019.

Fletcher Challenge Energy Taranaki, 1996. Awatea-1 Well Completion Report, PEP384557: New Zealand Geology (Survey unpublished open-file PR-2262).

Giba, M., Nicol, A., Walsh, J.J., 2010. Evolution of faulting and volcanism in a back-arc basin and its implication for subduction processes. Tectonophysics 29 (4), 1–18 TC4020.

Giba, M., Walsh, J.J., Nicol, A., 2012. Segmentation and growth of an obliquely reactivated normal fault. J. Struct. Geol. 39, 259–269.

Hansen, D.M., Cartwright, J., 2006. The three-dimensional geometry and growth of forced folds above saucer-shaped igneous sills. J. Struct. Geol. 28, 1520–1535.

Hansen, R.J., Kamp, P.J.J., 2008. New insights into the condensed nature and stratigraphic significance of the Late Neogene Ariki Formation, Taranaki Basin. N. Z. Pet. Conf. Proc. 1–13.

Hatherton, T., Davey, F.J., Hunt, T.M., 1979. Geophysical anomalies and igneous bodies off the west coast, North Island. J. R. Soc. N. Z. 9, 13–28.

Higgs, K.E., King, P.R., Raine, J.I., Sykes, R., Browne, G.H., Crouch, E.M., Baur, J.R., 2012. Sequence stratigraphy and controls on reservoir sandstone distribution in an Eocene marginal marine-coastal plain fairway, Taranaki Basin, New Zealand. Mar. Pet. Geol. 32, 110–137.

Hinton, G.E., Osindero, S., Teh, Y.W., 2006. A Fast Learning Algorithm for Deep Belief Nets. Neural Comput. 18, 1527–1554.

Höcker, C., Fehmers, G., 2002. Fast structural interpretation with structure-oriented filtering. Lead. Edge 21, 238–243.

Holford, S.P., Schofield, N., MacDonald, J.D., Duddy, I.R., Green, P.F., 2012. Seismic analysis of igneous systems in sedimentary basins and their impacts on hydrocarbon prospectivity: examples from the Southern Australian Margin. APPEA J. 52, 229–252.

Hornik, K., 1991. Approximation Capabilities of Multilayer Feedforward Networks. Neural Netw. 4, 251–257.

Infante-Paez, L., Marfurt, K.J., 2017. Seismic expression and geomorphology of igneous bodies. A Taranaki Basin, New Zealand case study. Interpretation 5, 1–72.

Jackson, C.A., Schofield, N., Golenkov, B., 2013. Geometry and controls on the development of igneous sill–related forced folds: A 2-D seismic reflection case study from offshore southern Australia. Geol. Soc. Am. Bull. 125, 1874–1890.

Jaglan, H., Qayyum, F., Huck, H., 2015. Unconventional seismic attributes for fracture characterization. First Break 33, 101–109.

Jiang, C., Chen, S., Zhang, E., Zhong, D., 2004. Methodology and Application of Seismic Prediction of Gas-bearing Volcanic Reservoir: Expanded Abstract. SEG Annual Meeting, Denver, pp. 1595–1598.

King, P.R., 2000. Tectonic reconstructions of New Zealand 40Ma to the present. N. Z. J. Geol. Geophy. 43, 611–638.

King, P.R., Thrasher, G.P., 1996. Cretaceous-Cenozoic Geology and Petroleum Systems of the Taranaki Basin. 13. Institute of geological and Nuclear Sciences, Lower Hutt (N.Z.) Monograph, New Zealand.

King, P.R., Naish, T.R., Browne, G.H., Field, B.D., Edbrooke, S.W., 1999. Cretaceous to Recent Sedimentary Patterns in New Zealand, Folio Series 1. Institute of Geological and Nuclear Sciences, Lower Hutt.

Kumar, P.C., Mandal, A., 2017. Enhancement of fault interpretation using multi-attribute analysis and artificial neural network (ANN) approach: a case study from Taranaki Basin, New Zealand. Explor. Geophys. 49, 409–424.

Kumar, P.C., Sain, K., 2018. Attribute amalgamation-aiding interpretation of faults from seismic data: an example from Waitara 3D prospect in Taranaki basin off New Zealand. J. Appl. Geophys. 159, 52–68.

Kumar, P.C., Omosanya, K.O., Sain, K., 2019. Sill Cube: An automated approach for the interpretation of magmatic sill complexes on seismic reflection data. Mar. Pet. Geol. 100, 60–84.

Liu, C., Liu, Y., Yang, B., Wang, D., Sun, J., 2006. A 2D multistage median filter to reduce random seismic noise. Geophysics 71, V105–V110.

Magee, C., Maharaj, S.M., Wrona, T., Jackson, C.A.L., 2015. Controls on the expression of igneous intrusions in seismic reflection data. Geosphere 11, 1024–1041.

Mathieu, L., De Vries, B.V.W., Holohan, E.P., Troll, V.R., 2008. Dykes, cups, saucers and sills: Analogue experiments on magma intrusion into brittle rocks. Earth Planet. Sci. Lett. 271, 1–13.

Meldahl, P., Heggland, R., Bril, B., de Groot, P., 1999. The Chimney Cube, an Example of Semi-automated Detection of Seismic Objects by Directive Attributes and Neural Networks: Part I; Methodology. Expanded Abstract. SEG Annual Meeting, pp. 931–934.

Meldahl, P., Bril, R.H.R., de Groot, P., Aminzadeh, F., 2002. Identifying Seismic Objects by their Texture, Orientation and Size: A New Interpretation Tool. Expanded Abstract, AAPG Annual Convention and Exhibition.

Onajite, E., 2014. Understanding noise in seismic record. Seismic Data Analysis Techniques in Hydrocarbon Exploration. Elsevier, Amsterdam, pp. 63–68.

Palmer, J.A., Andrews, P.R., 1993. Cretaceous-Tertiary sedimentation and implied tectonic controls on structural evolution of Taranaki Basin, New Zealand. South Pacific Sedimentary Basins: Sedimentary Basins of the World, 2. Elsevier, Amsterdam, pp. 309–328.

Pena, V., Chávez-Pérez, S., Vázquez-Garcia, M., Marfurt, K.J., 2009. Impact of shallow volcanics on seismic data quality in Chicontepec Basin, Mexico. Lead. Edge 28, 674–679.

Planke, S., Rasmussen, T., Rey, S.S., Myklebust, R., 2005. Seismic characteristics and distribution of volcanic intrusions and hydrothermal vent complexes in the Vøring and Møre basins. Petrol. Geol. Conf. Ser. Geolo. Soc., London 6, 833–844.
Polteau, S., Mazzini, A., Galland, O., Planke, S., Malthe-Sørenssen, A., 2008. Saucer-shaped intrusions: Occurrences, emplacement and implications. Earth Planet. Sci. Lett. 266, 195–204.
Poulton, M.M.ed., 2001. Computational neural networks for geophysical data processing. Elsevier 30.
Rateau, R., Schofield, N., Smith, M., 2013. The potential role of igneous intrusions on hydrocarbon migration, West Shetland. Pet. Geosci. 19, 259–272.
Rohrman, M., 2007. Prospectivity of volcanic basins: Trap delineation and acreage derisking. AAPG Bull. 91, 915–939.
Schutter, S.R., 2003. Hydrocarbon occurrence and exploration in and around igneous rocks. Geol. Soc. Lond. Spec. Publ. 7–33.
Seebeck, H.C., Nicol, A., Villamor, P., Ristau, J., Pettinga, J., 2014. Structure and kinematics of the Taupo Rift, New Zealand. Tectonics 33, 1178–1199.
Singh, D., Kumar, P.C., Sain, K., 2016. Interpretation of gas chimney from seismic data using artificial neural network: a study from Maari 3D prospect in the Taranaki basin, New Zealand. J. Nat. Gas. Sci. Eng. 36, 339–357.
Skogly, O., 1998. Seismic Characterization and Emplacement of Intrusives in the Voring Basin. [MS Thesis]. Norway, University of Oslo, Oslo.
Smallwood, J., Maresh, J., 2002. The properties, morphology and distribution of igneous sills: modelling, borehole data and 3D seismic from the Faroe-Shetland area. Geol. Soc. Lond., Spec. Publ. 197, 271–306.
Stagpoole, V., Funnell, R., 2001. Arc magmatism and hydrocarbon generation in the northern Taranaki Basin, New Zealand. Pet. Geosci. 7, 255–267.
Sun, Q., Wu, S., Cartwright, J., Wang, S., Lu, Y., Chen, D., Dong, D., 2014. Neogene igneous intrusions in the northern South China Sea: evidence from high-resolution three-dimensional seismic data. Mar. Pet. Geol. 54, 83–95.
Thomson, K., Hutton, D., 2004. Geometry and growth of sill complexes: insights using 3D seismic from the North Rockall Trough. Bull. Volcanol. 66, 364–375.
Thomson, K., Schofield, N., 2008. Lithological and structural controls on emplacement and morphology of sills in sedimentary basins: Structure and emplacement of high-level magmatic systems. Geol. Soc. Lond. Spec. Publ. 302, 31–44.
Tingdahl, K.M., 1999. Improving Seismic Detectability Using Intrinsic Directionality: Technical Report, B194. Earth Sciences Centre, Goteborg University.
Tingdahl, K.M., de Groot, P.F., 2003. Post-stack dip and azimuth processing. J. Seism. Explor. 12, 113–126.
Tingdahl, K.M., de Rooij, M., 2005. Semi-automatic detection of faults in 3D seismic data. Geophys. Prospect. 53, 533–542.
Zhang, K., Marfurt, K.J., Wan, Z., Zhan, S., 2011. Seismic attribute illumination of an igneous reservoir in China. Lead. Edge 30, 266–270.
Zou, C., 2013. Volcanic Reservoirs in Petroleum Exploration. 1st edn. Elsevier.
Zuo, G., Fan, G., 2011. A study of volcanic rocks identification by seismic methods in Subei Basin, Jiangsu Province, China. Paper presented at AAPG Annual Convention, Huston, Texas.